Supplementary Materials for

# Decoding Metal Cluster Stability and Evolution via a Geometry-Confined Superatomic Shell Model

Qiuying Du[1,3#], Weizhe Wang[1,2#], Shiquan Lin[1,2], Jijun Zhao[4], Shiv N. Khanna[5], Zhixun Luo[1,2*]

[1]Beijing National Laboratory for Molecular Sciences (BNLMS), State Key Laboratory for Structural Chemistry of Unstable and Stable Species, Institute of Chemistry, Chinese Academy of Sciences; Beijing 100190, China.

[2]School of Chemistry, University of Chinese Academy of Sciences; Beijing 100049, China.

[3]College of Physics and Electronic Information, Inner Mongolia Key Laboratory of Applied Condensed Matter Physics, Inner Mongolia Normal University; Hohhot 010022, China.

[4]Guangdong Provincial Key Laboratory of Quantum Engineering and Quantum Materials, School of Physics, South China Normal University; Guangzhou 510006, China.

[5]Department of Physics, Virginia Commonwealth University; Richmond, VA 23284-2000, USA.

*Corresponding author. Email: zxluo@iccas.ac.cn

[ξ] These authors contributed equally to this work.

## Contents

Materials and Methods ..... 2
Experimental methods ..... 2
Density functional theory methods ..... 2
Experimental Details ..... 14
Geometry and Energetics ..... 18
GCSS Model Analysis ..... 32
References ..... 47

# *Materials and Methods*

## Experimental methods

The instrumental setup employed in this work to acquire the research findings is based on self-designed equipment described in prior publications[57]. The experiments used a laser vaporization source with a gold disc target. A 532 nm laser beam struck the target surface, and a pulsed valve introduced high-purity helium carrier gas (99.999%, 10 atm) to entrain the resulting plasma. The plasma cooled before being injected into a growth chamber and passed through a supersonic nozzle ($\Phi$ = 2 mm, $L$ = 35 mm), where cluster growth occurred. The generated clusters were collimated by a skimmer and detected using a custom high-resolution reflection time-of-flight mass spectrometer (Re-TOFMS). Cluster size distribution was controlled by adjusting the laser Q-switch delay and carrier gas pulse width. The Re-TOFMS system comprised a pulsed acceleration field and a DC reflectron field, with product mass numbers determined from time-of-flight differences of ions with distinct mass-to-charge ratios.

For reaction studies, reactant gases were introduced into the growth chamber through a pulsed valve to react with the clusters. The resulting products were then carried by the carrier gas to the detection chamber for mass spectrometry analysis. By adjusting the pulse width of the carrier gas, different reactant concentrations could be achieved, enabling for controlled reactions of size-dependent gold clusters. Under conditions of low reactant gas concentration, the reactions between the gas molecules and gold clusters were approximated as pseudo-first-order processes. Based on this, the reaction rate constants for the gold clusters with $O_2$ and NO were determined.

## Density functional theory methods

Unbiased global structure searches for $Au_n^-$ clusters ($n$ = 7−20) are performed via a comprehensive genetic algorithm (CGA)[58] implemented in the DMol$^3$ package. For each cluster size, an initial population of sixteen randomly constructed geometries is adopted. In every evolutionary generation, new candidate structures are generated by crossover and mutation operations, each assigned an equal probability of 50%. A maximum of 5000 iteration steps is employed to guarantee convergence to the global minimum structure. All candidate configurations are further optimized at the DFT level using the all-electron relativistic approach with the PBE functional and DND basis set.

Low-energy isomers screened by the CGA method are further reoptimized with the Gaussian 16 program package[59]. The revTPSS functional together with the SDD basis set is adopted for Au atoms, whose reliability has been validated in our previous studies[60]. For the interactions of $Au_n^-$ clusters with $O_2$ and NO, all plausible adsorption sites—including top, bridge, and hollow sites—are fully considered. Both singlet and triplet spin states are evaluated for even-electron systems. The 6-311+G(*d*) basis set is applied to N and O atoms[61]. The HOMOs and LUMOs are also calculated with hybrid functional at the PBE0/SDD level of theory. Atomic charge distributions are obtained via natural population analysis (NPA)[62]. Electron density surfaces (EDSs) are calculated using the Multiwfn code, based on the electron density isosurface[63-65]. However, for smaller $Mg_n$ and $Al_n$ clusters with fewer atoms and smaller atomic radii, the compact geometry (e.g., tetrahedral 4-atom and triangular 3-atom geometries) renders the electron density surface more spherical. To better capture the actual confinement boundary, we therefore tested adjusted isosurface values for these systems, guided by the DFT-calculated orbital energy ordering as the benchmark: 0.006 a.u. for 4-atom clusters, 0.004 a.u. for 3-atom clusters, and 0.003 a.u. for 10-atom clusters. All molecular structure graphics are visualized and rendered by VMD software[66].

**GCSS model theory**

Originating in the late 1920s, Sommerfeld's free-electron theory describes electrons in a constant potential. Building on this picture, the nearly-free electron gas (NFEG) model introduces a weak periodic lattice perturbation; per Bloch's theorem, lattice-mediated Bragg scattering of electron waves opens band gaps at Brillouin-zone boundaries and yields band structures of nanocrystals. Further, spherical jellium models are developed to rationalize electronic shell structures in metal clusters and superatoms. Solving the single-particle Schrödinger equation for electrons confined within a spherical harmonic-oscillator ($V(r) = -V_0 + 1/2m\omega^2 r^2$, a square-well potential, or a mathematical Woods-Saxon potential $U(r) = -U_0/(1 + e^{\frac{r-r_0}{\epsilon}})$,[67] established a widely used criterion to predict magic numbers of metal clusters especially those of spherical geometry.

To rationalize the delocalized electrons in metal clusters of varying shapes and potentials, here we conduct complementary single-particle model calculations, for idealized infinite potential wells of diverse geometries: triangular, circular, rectangular, spherical, ellipsoidal, tetrahedral ($T_d$), icosahedral ($I_h$), octahedral ($O_h$), cuboctahedral ($O_h$), regular triangular prism ($D_{3h}$) and the regular triangular pyramid ($C_{3v}$) boundaries as well as boundaries from DFT electron-density cube. The

confinement potentials for all cases are obtained via solutions to the particle-in-a-box Schrödinger equations, which are implemented within the MATLAB environment. The core idea of the model is as follows:

We represent each delocalized electron as an independent particle confined to a domain $\Omega$ and solve the stationary Schrödinger equation with the bare electron mass $m_e$:

$$\begin{gathered}\widehat{H}\psi_i(\vec{r}) = \left[-\frac{\hbar^2}{2m_e}\nabla^2 + V_\Omega(\vec{r})\right]\psi_i(\vec{r}) = E_{phys_i}\psi_i(\vec{r}) \\ V_\Omega(\vec{r}) = \begin{cases} 0 & if\ \vec{r} \in \Omega \\ +\infty & if\ \vec{r} \notin \Omega \end{cases}\end{gathered} \tag{1}$$

The infinite barrier imposes a homogeneous Dirichlet condition. The domain is defined either by a prescribed analytical geometry, $\Omega_g$, rasterized by an interior-exterior mask, or directly from a DFT electron-density cube, $\Omega_\rho$. In the latter case, the density threshold is supplied explicitly or taken as the median cube density interpolated at the Multiwfn surface vertices:

$$\psi_i(\vec{r})|_{\vec{r}\in\partial\Omega} = 0, \Omega = \Omega_g \text{ or } \Omega_\rho = \{\vec{r}: \rho(\vec{r}) \geq \rho_{\text{iso}}\} \tag{2}$$

Idealized 3D shapes are rescaled to the same target volume, $|\Omega| = 4\pi R_0^3/3$, and energies are reported in the equal-volume dimensionless unit E*,

$$\begin{gathered}E_i(\mathrm{E}^*) = E_{phys_i} \cdot \frac{2m_e R_0^2}{\pi\hbar^2} \\ R_0 = \left(\frac{3|\Omega|}{4\pi}\right)^{\frac{1}{3}}\end{gathered} \tag{3}$$

**Analytical benchmarks**

Specifically, the single-particle Schrödinger equation with an infinite potential well can be solved analytically for several canonical geometries: the 2D equilateral triangle, square, and circle, as well as the 3D sphere, yielding energy eigenvalues $E$ (see below for the corresponding energy levels for each geometry).

Idealized 2D shapes are rescaled to the same target area $|A|$, and energies are reported in the equal-area dimensionless unit E*,

$$E_i(\mathrm{E}^*) = E_{phys_i} \cdot \frac{2m_e|A|}{\pi^2\hbar^2} \tag{4}$$

Dimensionless energies for a single-particle in equilateral triangular well are given by single-particle in equilateral triangular well:[68]

$$E_{p,q}(\mathrm{E}^*) = \frac{4\pi^2\hbar^2}{2m_e(\frac{\sqrt{3}a}{2})^2} \cdot \frac{2m_e\frac{\sqrt{3}}{4}a^2}{\pi^2\hbar^2}(p^2+pq+q^2) = 2.309(p^2+pq+q^2) \tag{5}$$

where $p$ and $q$ are quantum numbers depend on irreducible representations:

$$q = \begin{cases} 0,1,2,\dots, & \text{for } \mathrm{A}_1 \\ 1,2,3,\dots, & \text{for } \mathrm{A}_2 \\ \frac{1}{3},\frac{2}{3},\frac{4}{3},\frac{5}{3},\dots, & \text{for } E \end{cases} \qquad p = q+1, q+2, \dots \tag{6}$$

The dimensionless energies for a single-particle in square well are given by:

$$E_{n_x,n_y}(\mathrm{E}^*) = \frac{\pi^2\hbar^2}{2m_e a^2} \cdot \frac{2m_e a^2}{\pi^2\hbar^2}\left(n_x^2+n_y^2\right) = n_x^2+n_y^2 \tag{7}$$

where $n_x$ and $n_y$ are quantum numbers:

$$n_x, n_y = 1,2,3,\dots \tag{8}$$

The dimensionless energies for a single-particle in circular well are given by:

$$E_{n,l}(\mathrm{E}^*) = \frac{\alpha_{n,l}^2\hbar^2}{2m_e R_0^2} \cdot \frac{2m_e\pi R_0^2}{\pi^2\hbar^2} = \frac{\alpha_{n,l}^2}{\pi} \tag{9}$$

where $\alpha_{n,l}$ represents the $n^{\text{th}}$ root of the Bessel function of the first kind $J_l(\alpha_{n,l}) = 0$; $n$ and $l$ are principal quantum number and the angular quantum number, respectively.

The dimensionless energies for a single-particle in spherical well are obtained exactly from the zeros $\tau_{n,l}$ of the spherical Bessel function $j_l(\tau_{n,l})$, giving:

$$E_{n,l}(\mathrm{E}^*) = \frac{\tau_{n,l}^2 \hbar^2}{2m_e R_0^2} \cdot \frac{2m_e R_0^2}{\pi \hbar^2} = \frac{\tau_{n,l}^2}{\pi} \tag{10}$$

In this case, ($n$, $l$, $m$) are exact quantum numbers and each shell with angular momentum $l$ exhibits the exact ($2l$ + 1) fold of degeneracy.

**Ellipsoidal wells**

For the axisymmetric ellipsoidal wells, cylindrical coordinates $(\rho, \phi, z)$ are a natural choice because the system is invariant under rotations about the $z$-axis. In these coordinates, the Laplacian separates the azimuthal angle $\phi$ from the radial and axial coordinates, allowing the wavefunction to be written as:

$$\psi(\rho, \phi, z) = u_m(\rho, z)\, exp(\, im\phi) \tag{11}$$

The boundary of the ellipsoid is given by:

$$\text{Oblate: } \left(\frac{\rho}{a}\right)^2 + \left(\frac{z}{c}\right)^2 \leq 1; \text{ Problate: } \left(\frac{\rho}{c}\right)^2 + \left(\frac{z}{a}\right)^2 \leq 1 \tag{12}$$

where $a$ and $c$ denote the semi-major and semi-minor axes of the ellipsoidal confining potential, respectively.

This boundary is independent of $\phi$ and thus is simple to implement in cylindrical coordinates. This choice reduces the 3D problem to a set of 2D problems (one for each $m$), greatly reducing computational cost while preserving the exact quantum number $m$.

In addition, the calculations are performed under the fixed-volume constraint:

$$\text{Oblate: } V = \frac{4}{3}\pi a^2 c = \frac{4}{3}\pi R_0^3 \rightarrow a^2 c = R_0^3; \text{ Prolate: } V = \frac{4}{3}\pi a c^2 = \frac{4}{3}\pi R_0^3 \rightarrow a c^2 = R_0^3 \quad (13)$$

A conservative finite-difference discretization in cylindrical coordinates then leads to a generalized eigenvalue problem:

$$Ku = \lambda Mu \quad (14)$$

where the matrices *K* and *M* arise from the finite-difference discretization of the operator $-\nabla^2$ and the volume element $\rho d\rho dz$, respectively, and $u$ is the discrete eigenvector containing the values of $u_m(\rho, z)$ at the grid points. In the deformed ellipsoidal wells, the pair $\pm m$ remains exactly degenerate for $m > 0$, whereas the additional $z$-to-$-z$ parity is used to distinguish even and odd branches within a given $m$ sector. The labels ($n$, $l$, $m$) used in the plots therefore indicate the spherical parent state at the undeformed limit and are tracked continuously along the deformation coordinate, rather than representing exact conserved quantum numbers away from the spherical point. Our model produces results consistent with the perturbative theory calculations documented in the literature [69], as illustrated by our MATLAB code.

**Cartesian-grid discretization and normalization**

For Cartesian-grid solvers, the computational domain was represented by the retained grid nodes. Analytical domains were rasterized by their inside–outside tests. Density-defined nodes were retained when $\rho(x, y, z) \geq \rho_{iso}$.

For directional spacings *dx*, *dy*, and *dz*, the discrete negative Laplacian acting on $c_{ijk}$ was written as follows. Here, c̃ equals the neighbouring coefficient inside the mask and zero outside it.

$$\begin{aligned}(Ac)_{ijk} = {} & 2(dx^{-2} + dy^{-2} + dz^{-2})c_{ijk} \\ & -dx^{-2}(\tilde{c}_{i-1,j,k} + \tilde{c}_{i+1,j,k}) \\ & -dy^{-2}(\tilde{c}_{i,j-1,k} + \tilde{c}_{i,j+1,k}) \\ & -dz^{-2}(\tilde{c}_{i,j,k-1} + \tilde{c}_{i,j,k+1}),\end{aligned} \quad (15)$$

All six directional terms were retained on the diagonal, while an off-diagonal term was added only for an internal neighbour. For $dx = dy = dz = f$, the diagonal becomes $\frac{6}{f^2}$ and each retained neighbour contributes $-\frac{1}{f^2}$.

This construction is a voxelized, zero-ghost-value approximation to the Dirichlet problem. The analytical boundary is replaced by a staircase surface, and no cut-cell or sub-voxel boundary correction was applied. The interior stencil is second order, but boundary-position errors remain grid dependent and can affect low- and high-energy states.

The lowest eigenpairs were obtained with MATLAB eigs. The calculations used a tolerance of $10^{-10}$ and at most 3,000 iterations. The smallest-real option was attempted first, with smallest-absolute-value used as a fallback where implemented.

For a unit-edge analytical well, $\lambda_i$ was converted using the equal-volume edge $a_{\mathrm{eq}}$. For a density grid expressed in physical coordinates, $\lambda_i$ directly represents $k_i^2$.

$$Ac_i = \lambda_i c_i, k_i^2 = \frac{\lambda_i}{a_{\mathrm{eq}}^2}, E_i(E^*) = \frac{k_i^2 R_0^2}{\pi}. \tag{16}$$

Cartesian eigenvectors used for overlaps, projections, and character traces were Euclidean orthonormal on the retained nodes. This convention differs from volume normalization by the state-independent factor $(dxdydz)^{-\frac{1}{2}}$ on a uniform grid.

The $C_{3v}$ triangular-pyramid and $D_{3h}$ triangular-prism scripts applied this factor to separate plotting copies. Other Cartesian scripts retained Euclidean-normalized vectors because relative isovalues and subspace rankings are unchanged by an overall scale. The cylindrical ellipsoid solver instead used its radial weight matrix $M$ for normalization.

Accordingly, $|\psi_i|^2$ is interpreted as a single-particle probability-density pattern, not a many-electron density. Within a degenerate multiplet, an individual signed isosurface represents one numerical orthonormal basis and is not uniquely defined.

**Polyhedral wells**

The regular tetrahedron was rasterized by barycentric coordinates. The octahedral mask satisfied $|x| + |y| + |z| \leq \frac{1}{\sqrt{2}}$. Cuboctahedral and icosahedral masks used convex-hull half-space inequalities generated from their vertices.

The equilateral-base triangular pyramid used convex-face inequalities. The triangular prism combined a barycentric triangular cross-section with $-\frac{h}{2} \leq z \leq \frac{h}{2}$, where h is the prism height.

The $T_d$, $O_h$ and $I_h$ scripts grouped low-lying states before evaluating symmetry characters. $T_d$, and $O_h$ used a seed-based tolerance of $10^{-6}$. $I_h$ used $2 \times 10^{-5}$, followed by its documented $5 \times 10^{-3}$ adjacent-group merge heuristic.

The $C_{3v}$ triangular-pyramid and $D_{3h}$ triangular-prism scripts followed a different procedure. They classified individual eigenvectors from normalized $C_3$ and mirror overlaps, using a tolerance of 0.35, without first forming degenerate subspaces.

Spherical-Bessel and real-spherical-harmonic descriptor functions were sampled on the retained nodes and orthonormalized to form $\Phi_{nl}$. The radial expression was evaluated across the full non-spherical domain, including nodes with $r > R_0$. It is therefore an analytically extended descriptor basis, rather than a compactly supported spherical-well eigenbasis.

$$(n, l)_g = \underset{n,l}{\operatorname{argmax}} \frac{\|\Phi_{nl}^{\dagger} \Psi_g\|_F^2}{d_g} \tag{17}$$

For the ideal $T_d$ and $O_h$ solvers, the projection term in Eq. (17) was combined with energetic proximity and irreducible-representation compatibility. Energy-ordered groups were then matched one-to-one to compatible spherical-shell slots by a global monotonic assignment.

The $I_h$ solver instead used the largest unweighted subspace projection. The $C_{3v}$ triangular-pyramid and $D_{3h}$ triangular-prism scripts did not implement this spherical-parent projection. Their reported labels were based on symmetry overlaps, parity, morphology, and nodal patterns.

The density-cube solver assigned spherical-parent labels to individual eigenvectors before energy grouping, using $l \leq 6$ and $n \leq 4$. These labels can change under an orthogonal rotation within a degenerate subspace. They were therefore used only as basis-dependent display descriptors and not for irreducible-representation assignment.

**Electron density-defined wells**

Cluster-specific domains were constructed from one scalar-density cube on an axis-aligned Cartesian grid. Cube and vtx.txt coordinate units were declared independently as Bohr or angstrom. Bohr coordinates were multiplied by 0.529, while density values remained in the native cube units.

In from_vtx mode, duplicate surface vertices were removed before trilinear interpolation of the cube density. Only finite, in-grid interpolants were retained, and $\rho_{\mathrm{iso}}$ was their median. In manual mode, the supplied $\rho_{\mathrm{iso}}$ had to use the native cube-density units, and vtx.txt was not read.

The confinement mask contained every node satisfying $\rho \geq \rho_{\mathrm{iso}}$. No alpha-shape fit, analytical surface fit, connected-component filter, or automatic check for contact with the cube boundary was applied.

The grid-sum volume, equal-volume sphere radius $R_0$, and PCA half-ranges were calculated as follows. In from_vtx mode, PCA used the retained surface vertices. Manual mode used the six-neighbour boundary nodes of the mask.

$$V \approx N_{\mathrm{in}} dxdydz, R_0 = (\frac{3V}{4\pi})^{\frac{1}{3}},$$
$$\frac{x}{h} = 1.35\frac{a}{c} \text{(empirical mapping used for Fig. 4c upon calculation in Fig. S30).} \quad (18)$$

Each PCA half-range was one-half of the projected coordinate range along a principal direction. The three values were sorted as $a \geq b \geq c$, and $\frac{a}{b}$, $\frac{b}{c}$, and $\frac{a}{c}$ were reported. This sorting removes the identities of the axial and in-plane directions, so $\frac{a}{c}$ is a maximum-to-minimum anisotropy descriptor.

For an equilateral base (Fig. 4d), the geometric relation $\frac{x}{h} = \frac{2}{\sqrt{3}}(\frac{H_\Delta}{h})$ applies only after the base altitude $H_\Delta$ and axial height $h$ are identified. For Fig. 4c, $\frac{x}{h} = 1.35\frac{a}{c}$ was retained as a fixed empirical calibration obtained during main-text figure testing. The coefficient was not generated by the MATLAB script and was not refitted for individual clusters.

Starting from the first unassigned state $k$, later states $j$ were included while $|E_j(E^*) - E_k(E^*)| \leq 5 \times 10^{-3}\max(|E_k(E^*)|,1)$. The tolerance was referenced to the first state of each block and was not applied transitively to adjacent spacings.

**Symmetry analysis**

Spatial operations were inferred from the atomic coordinates in the cube header, not from the thresholded density mask. Coordinates were centered at their arithmetic mean before candidate operations were tested by element-preserving atom matching.

The search considered $C_n$ rotations for $n$ = 2–6, inversion, mirror planes, and $S_n$ operations for $n$ = 4, 6, 8, 10, and 12. The maximum atomic matching error was 0.30 Å. At most 2,500 candidate axes were examined, merged at 0.10°, and clustered at 5.0°.

Accepted generators were expanded into the finite operation set used for character analysis. For each preliminary energy block g, the numerical vectors formed the columns of $\Psi_g$.

$$\begin{gathered}\Psi_g = [\psi_1, \dots, \psi_{d_g}], \Psi_g^\dagger \Psi_g = I_{d_g}, \\ D_g(S_a) = \Psi_g^\dagger U(S_a) \Psi_g, \chi_g(S_a) = \mathrm{ReTr}[D_g(S_a)].\end{gathered} \tag{19}$$

Each operation acted through trilinear interpolation of a full-grid wavefunction that was zero outside $\Omega$. Out-of-grid and non-finite interpolation values were also set to zero. Closure within the tested subspace was quantified by the normalized leakage.

$$L_g = \max_a \left[ \frac{max\{\|U(S_a)\Psi_g\|_F^2 - \|D_g(S_a)\|_F^2, 0\}}{max\{\|U(S_a)\Psi_g\|_F^2, \varepsilon_{\mathrm{mach}}\}} \right]^{\frac{1}{2}} \tag{20}$$

Small negative numerators caused by round-off were clipped to zero, and the denominator was bounded by machine precision. $L_g$ measures the retained transformed norm outside the tested subspace. It does not measure total norm lost through interpolation or domain truncation.

Candidates with the same dimension as the numerical block were ranked by the class-weighted root-mean-square character mismatch.

$$\begin{gathered}R_{g,\Gamma} = \left[ \frac{\sum_a w_a |\tilde{\chi}_g(S_a) - \chi_\Gamma(S_a)|^2}{\sum_a w_a} \right]^{\frac{1}{2}} \\ \Gamma^* = \underset{\Gamma : d_\Gamma = d_g}{\mathrm{argmin}} R_{g,\Gamma}\end{gathered} \tag{21}$$

Finite axial groups sampled all generated elements with unit weights. Polyhedral groups sampled one adopted real-character-table representative per class and used the theoretical class multiplicity. Linear groups used a $D_{13}$ surrogate with $|m| \leq 6$ and did not permit exact-tier assignments.

For T and $\underline{T_h}$, conjugate complex one-dimensional species were combined into two-dimensional real E species. The best candidate was unique only when its mismatch differed from the next candidate by more than $10^{-8}$.

An exact numerical label required both $R_{g,\Gamma^*} \leq 0.15$ and $L_g \leq 0.15$ where exact-tier assignment was enabled. An approximate label required both quantities to be at most 0.35. Otherwise, no irreducible-representation label was forced.

A two- to eight-state block could be recursively partitioned when it failed the single-irrep test and its whole-block leakage did not exceed 0.35. Allowed subset dimensions were tested, and every retained subset had to pass the same matching criteria

$$J(P) = \sum_{p \in P} [R_{p,\Gamma_p} + 0.25 L_p]$$
$$R_{\text{decomp}} = \left[ \frac{\sum_a w_a |\chi_g(S_a) - \sum_{p \in P} \chi_{\Gamma_p}(S_a)|^2}{\sum_a w_a} \right]^{\frac{1}{2}} \leq 0.35 \tag{22}$$

The accepted partition minimized *J(P)* and also required $R_{\text{decomp}} \leq 0.35$. This procedure partitions the eigensolver columns heuristically. It does not rotate the block into projection-operator-derived symmetry-adapted linear combinations.

**Visualization and numerical limitations**

Visualization settings were script specific. The $C_{3v}$ triangular-pyramid and $D_{3h}$ triangular-prism plots used signed isosurfaces at $\pm 0.28 \max|\psi|$ and included a central density slice. The cuboctahedral, icosahedral, and density-cube plots used $\pm 0.35 \max|\psi|$ without that slice.

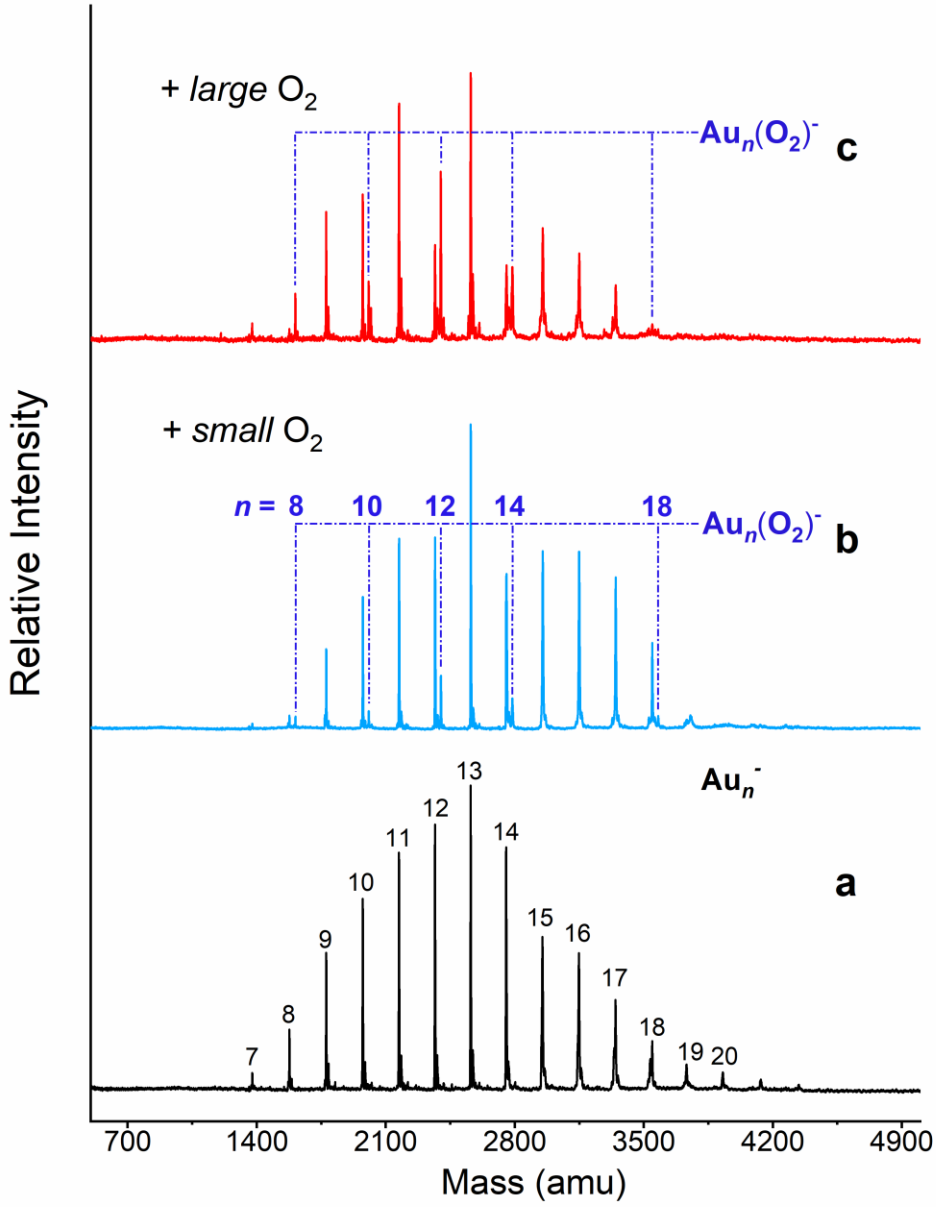
Signed surfaces preserve the phase of the displayed numerical vector. However, individual vectors within a degenerate multiplet are arbitrary up to an orthogonal basis change. Subspace characters, projection weights, and summed multiplet densities are basis invariant.

Each cube run should retain $\rho_{iso}$, both unit flags, $dx$, $dy$, $dz$, $N_{in}$, $V$, $R_0$, the PCA ranges, point group, tolerances, and script version. The CSV exporter omits some fields, so they must be preserved with the run configuration and console record.

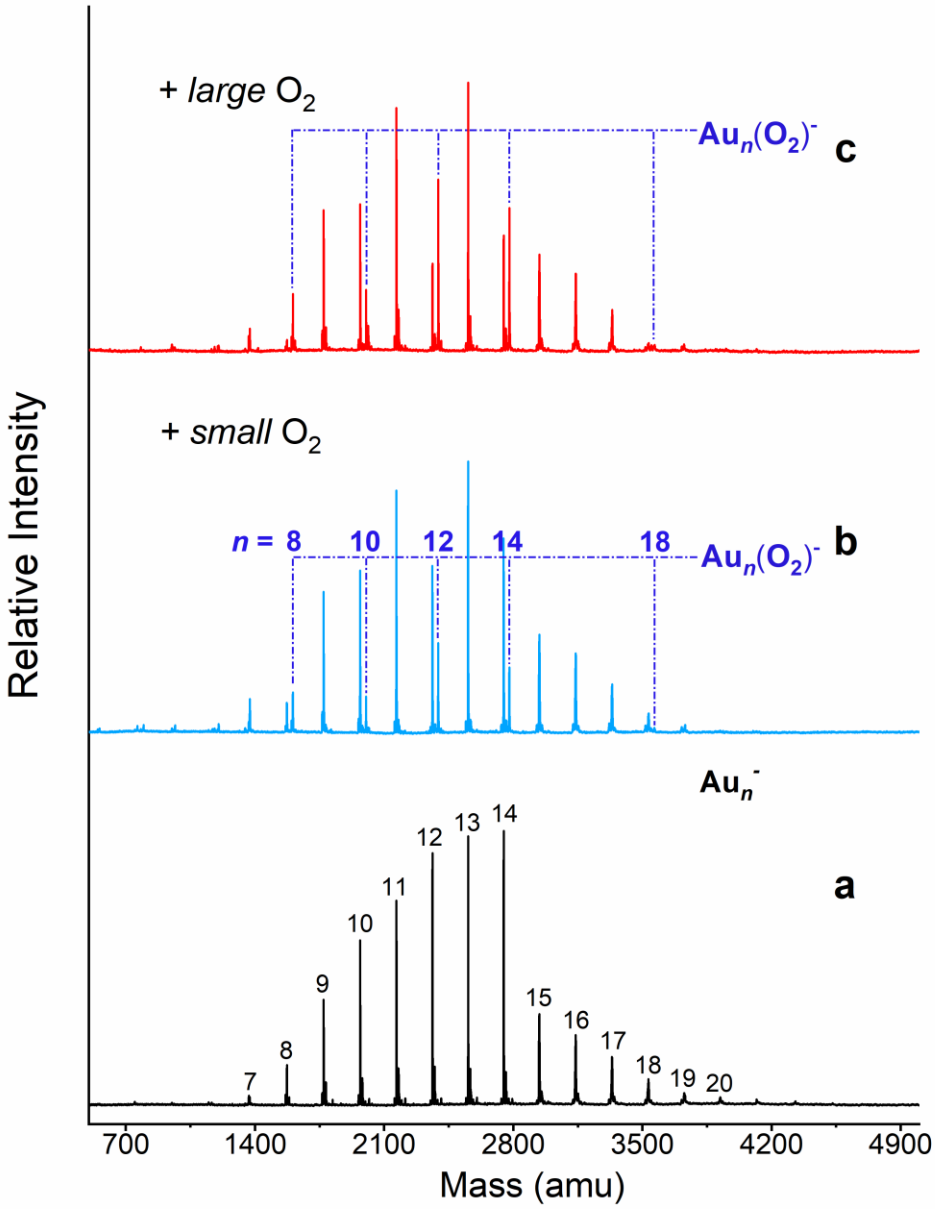
These calculations were used to identify robust trends in shell ordering and symmetry-driven level splitting. Absolute eigenvalues retain grid and staircase-boundary errors, including at low energy. In addition, for potentials that are strongly deformed from spherical symmetry, the resulting spherical $n$ and $l$ labels should therefore be regarded only as approximate references, and definitive assignment of a specific superatomic orbital requires manual judgement based on the orbital shape and nodal pattern.

***Further details regarding the GCSS model are available in the MATLAB codes deposited on Zenodo (DOI: 10.5281/zenodo.22127728).***

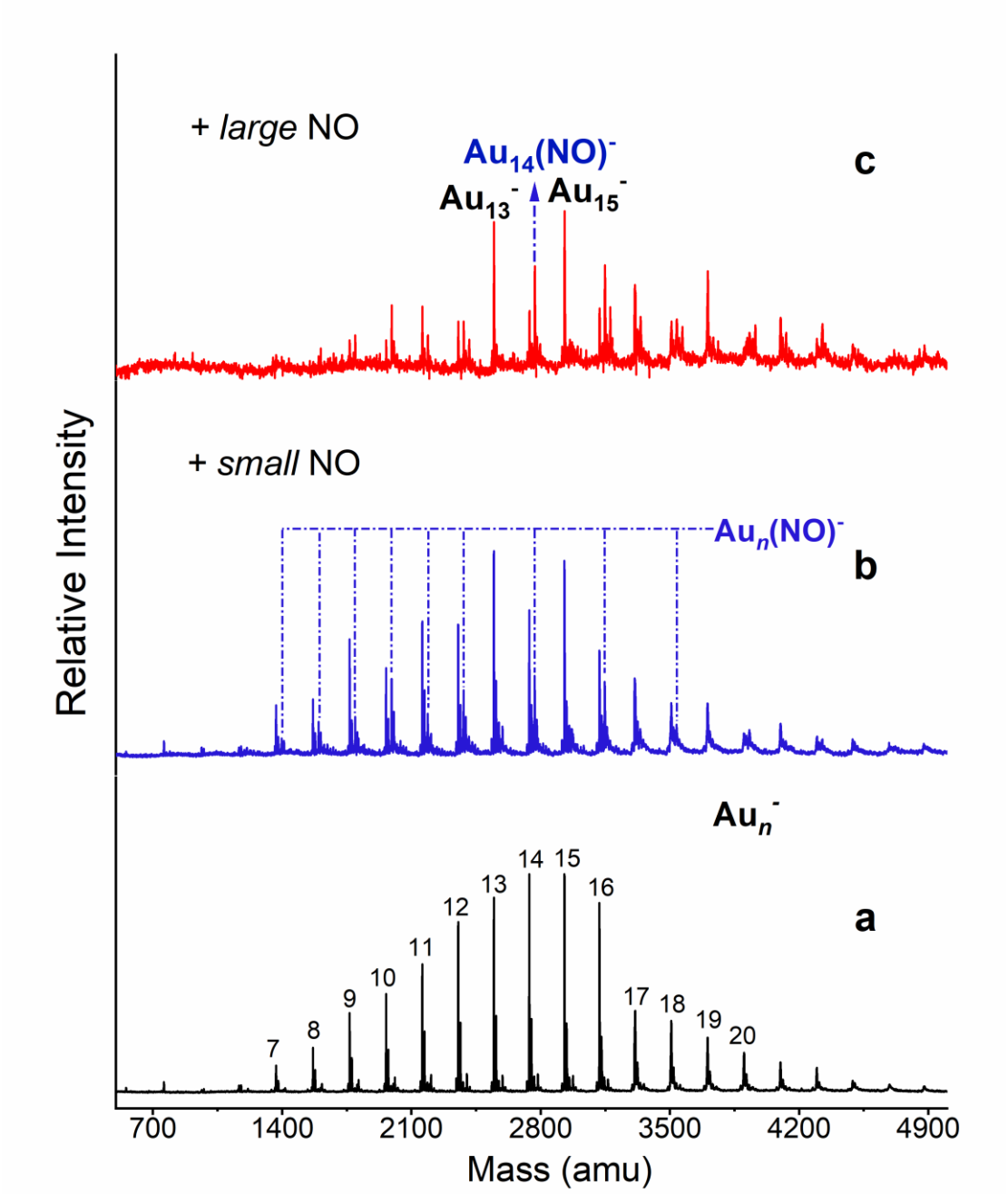
# *Experimental Details*



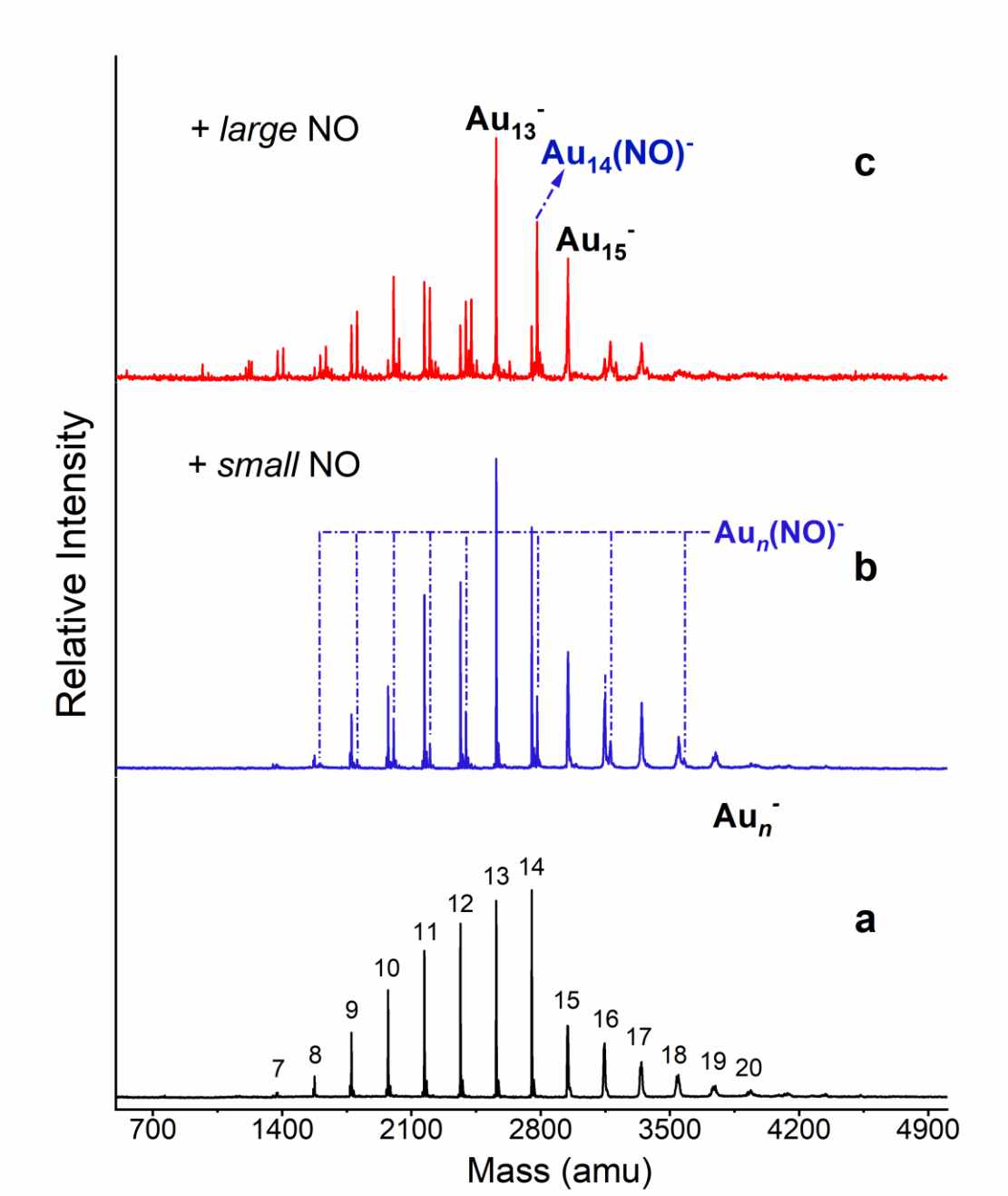

**Supplementary Fig. 1 | Mass spectroscopy of $Au_n^-$ clusters reacting with $O_2$. a–c,** Mass distribution of $Au_n^-$ clusters ($n$ = 7−20) (**a**) produced by the Lava source with a 35 mm-long nozzle at He gas pressure of 10 atm, and after reacting with $O_2$ (5% in He, 1 atm). The small (**b**) and large (**c**) doses of the reactant correspond to pulsed (10 Hz) widths at 180 μs and 205 μs, respectively.



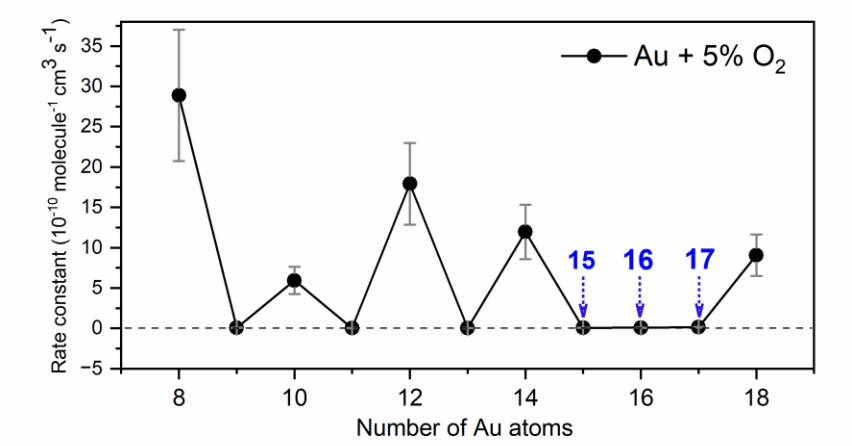

**Supplementary Fig. 2 | Repeat experiments of $Au^-$ clusters reacting with $O_2$. a–c**, Mass distribution of $Au_n^-$ clusters ($n$ = 7−20) (**a**) produced by the Lava source with a 35 mm-long nozzle at He gas pressure of 10 atm. The small (**b**) and large (**c**) $O_2$ (5% in He, 1 atm) doses of the reactant correspond to pulsed (10 Hz) widths at 180 μs and 205 μs, respectively.




**Supplementary Fig. 3 | Repeat experiments of $Au_n^-$ clusters reacting with NO. a–c**, Mass distribution of $Au_n^-$ clusters ($n$ = 7–20) (**a**). The NO reactant (5% in He, 1 atm) of small (**b**) and large (**c**) doses corresponding to pulsed (10 Hz) widths at 180 μs, and 225 μs, respectively.

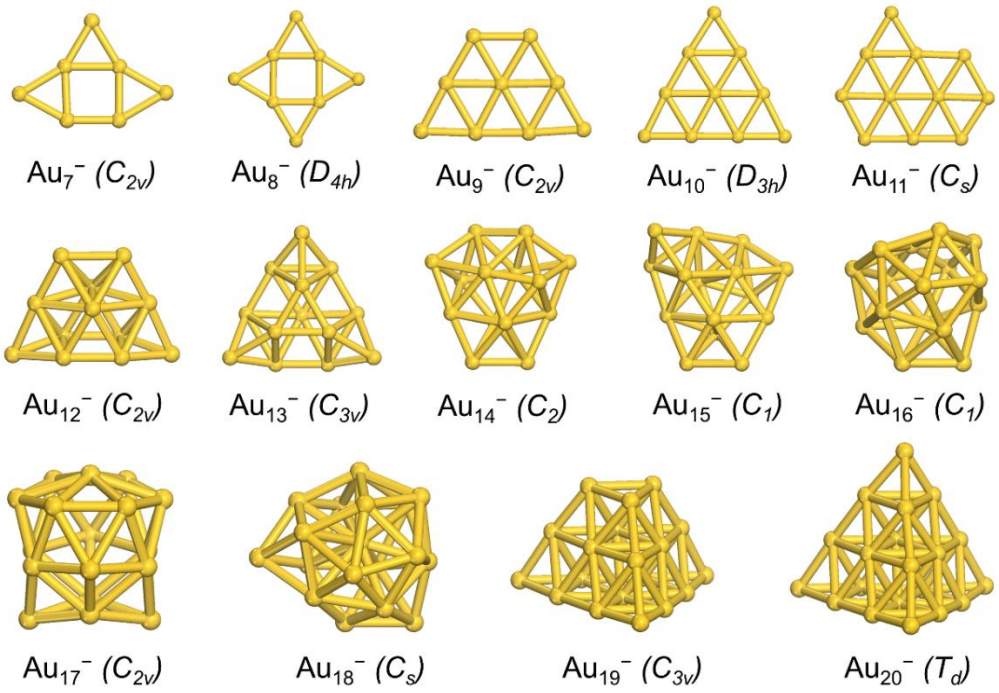



**Supplementary Fig. 4 | Repeat experiments of $Au_n^-$ clusters reacting with NO**. **a-c**, Mass distribution of the nascent $Au_n^-$ clusters (**a**) and after reacting with NO (5% in He, 1 atm) with small (**b**), and large (**c**) doses corresponding to pulsed (10 Hz) widths at 180 μs and 215 μs, respectively.

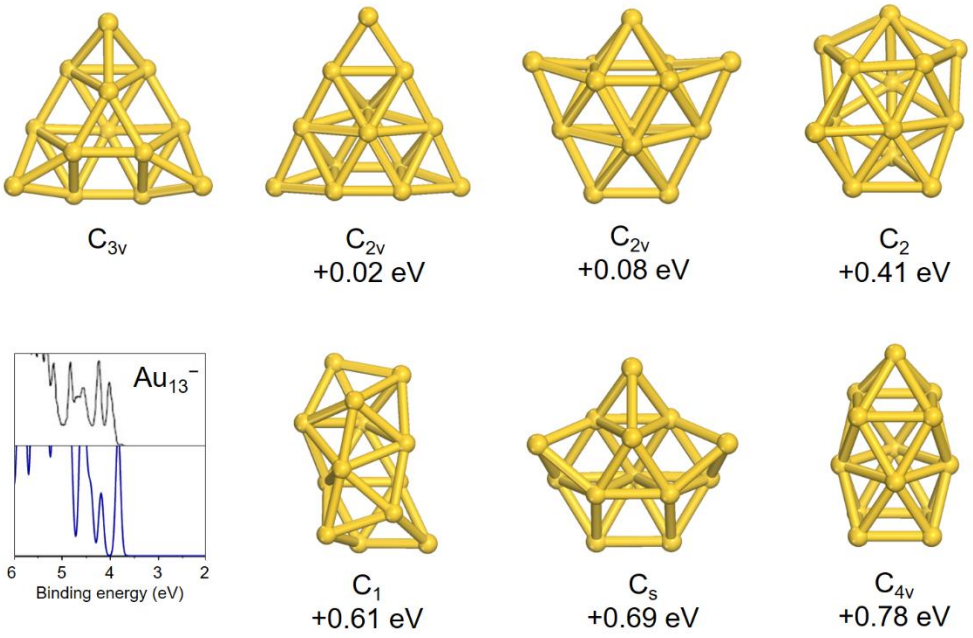



**Supplementary Fig. 5 | Reaction rate estimation.** The experimentally determined reaction rate constants of $Au_n^-$ ($n$ = 7–21) clusters with 180 μs $O_2$ (5% in He, 1 atm).

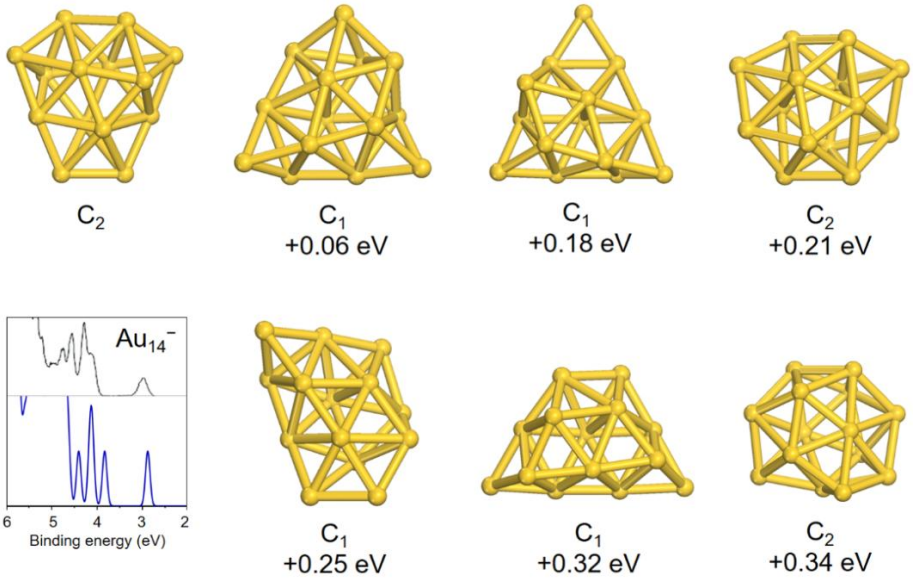
# *Geometry and Energetics*



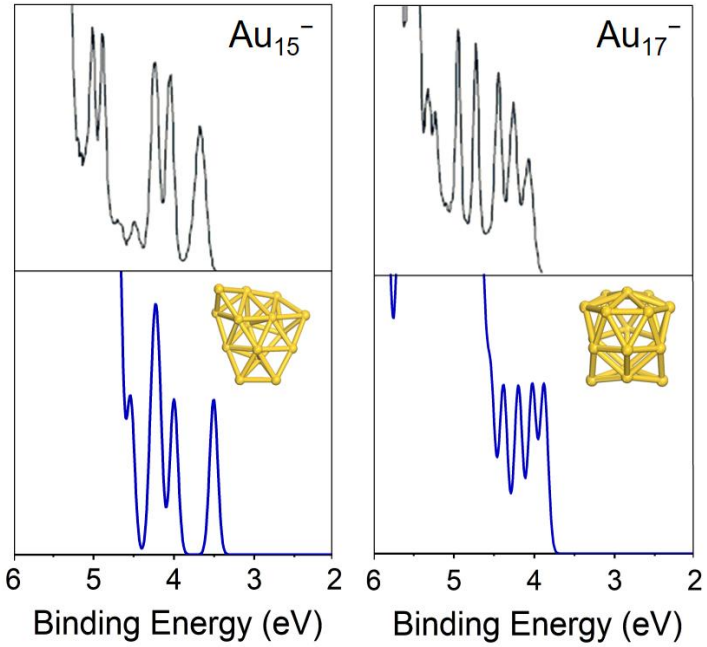

**Supplementary Fig. 6 | Optimized structures of $Au_n^-$ clusters.** The DFT-optimized structures of $Au_n^-$ ($n$ = 7−20) clusters.



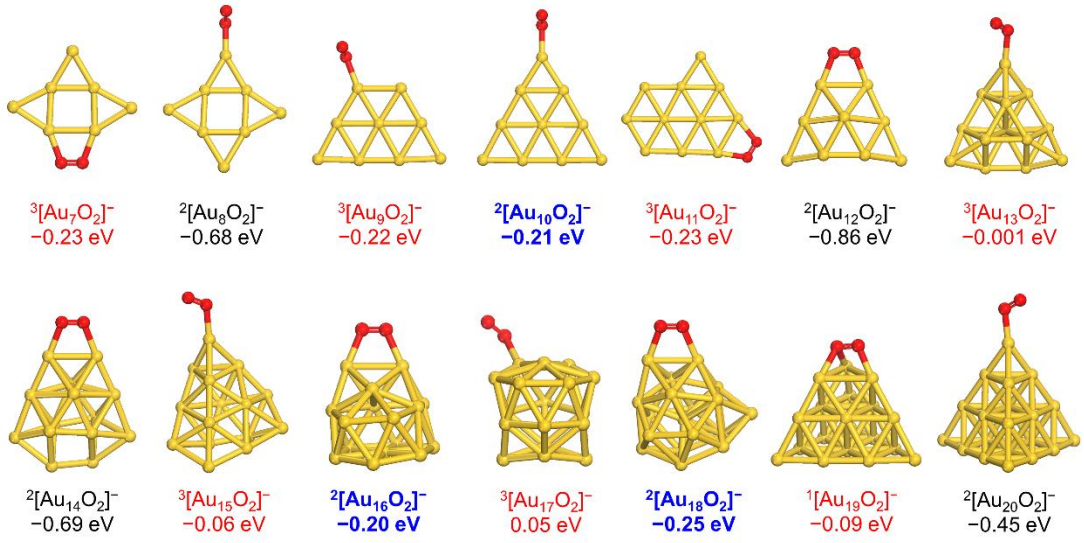

**Supplementary Fig. 7 | Ground-state and low-energy isomers of the $Au_{13}^-$ cluster**. The energy differences between each isomer and the ground state are given in the second row. The inset shows the simulated (blue curve) photoelectron spectrum of the lowest-energy $Au_{13}^-$ cluster, in comparison with the previous experimental result (black curve)[70-72].



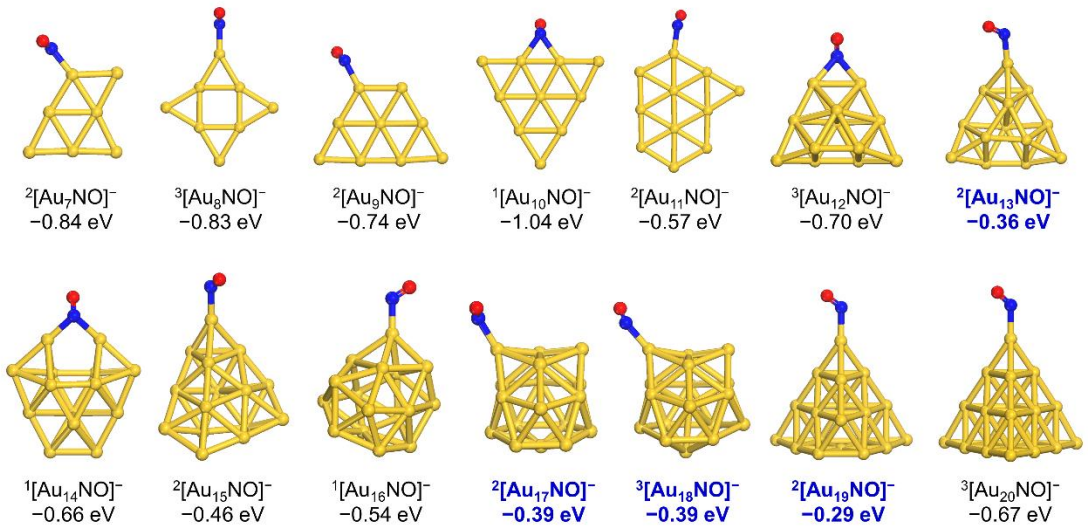

**Supplementary Fig. 8 | Ground-state and low-energy isomers of the $Au_{14}^-$ cluster**. The energy differences between each isomer and the ground state are given in the second row. The inset shows the simulated (blue curve) photoelectron spectrum of the lowest-energy $Au_{13}^-$ cluster, in comparison with the previous experimental result (black curve)[70-72].



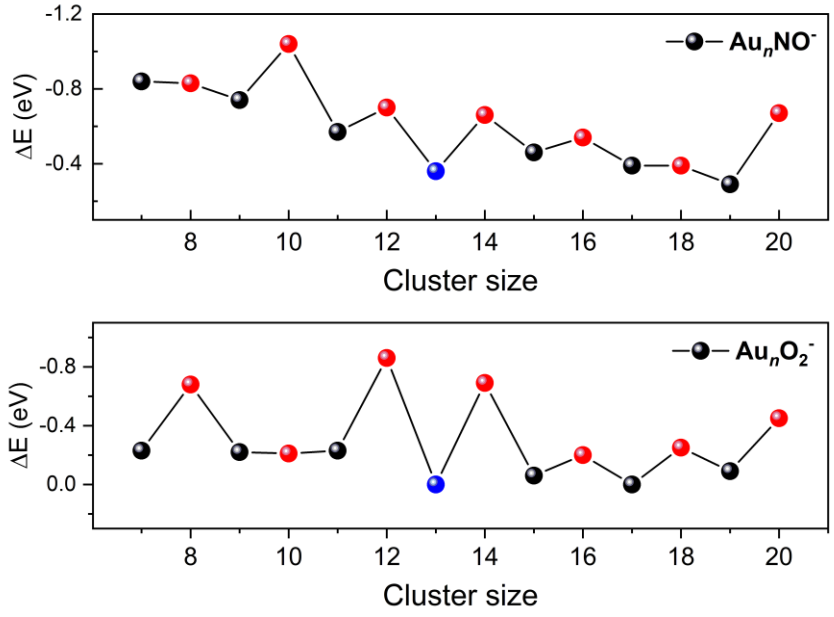

**Supplementary Fig. 9 | Photoelectron spectra of the $Au_{15}^-$ and $Au_{17}^-$ clusters**. The simulated (blue curve) photoelectron spectrum of the lowest-energy $Au_{15}^-$ and $Au_{17}^-$ clusters, in comparison with the previous experimental result (black curve)[70-72].



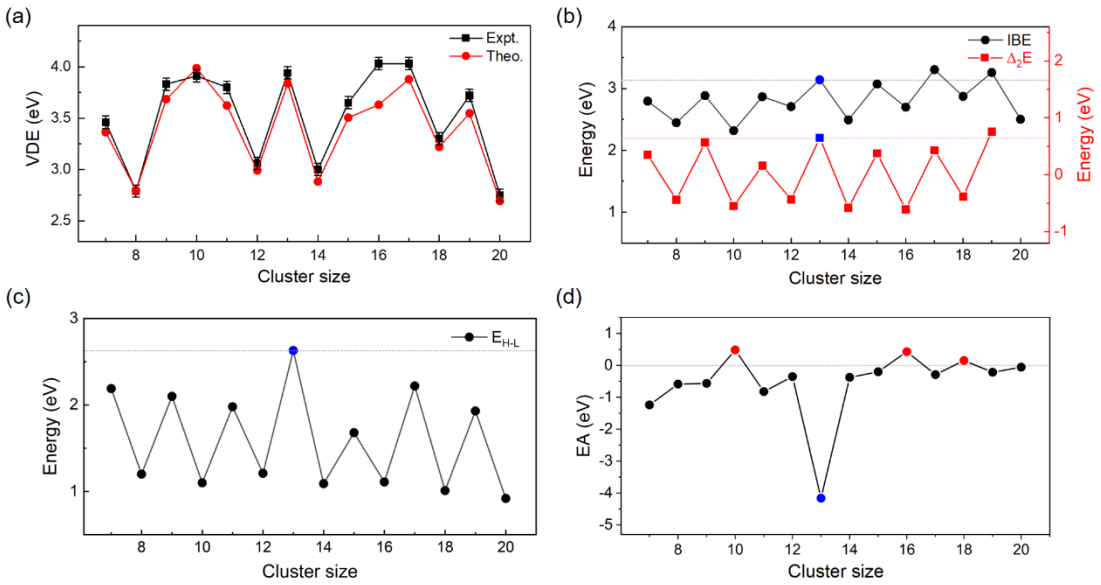

**Supplementary Fig. 10 | Optimized structures of $Au_nO_2^-$**. The DFT-optimized structures, spin multiplicities, and adsorption energies of $O_2$ on $Au_n^-$ ($n$ = 7−20) clusters.




**Supplementary Fig. 11 | Optimized structures of Au$_n$NO$^-$.** The DFT-optimized structures, spin multiplicities, and adsorption energies of NO on Au$_n^-$ ($n$ = 7−20) clusters.




**Supplementary Fig. 12 | Adsorption energy. DFT-calculated O$_2$- and NO-adsorption energies** on the Au$_n^-$ ($n$ = 7–20) clusters.




**Supplementary Fig. 13 | The electronic properties of $Au_n^-$ clusters. a**, The DFT-calculated vertical detachment energies (VDE) of $Au_n^-$ ($n$ = 7–20) clusters (**a**), in comparison with the experimental results.[70-73] **b,** Calculated incremental binding energies (IBE) and second-order difference in binding energy ($\Delta_2E$) of $Au_n^-$ ($n$ = 7−20) clusters. **c**, DFT-calculated HOMO-LUMO gaps ($E_{H-L}$) and HOMO-LUMO for alpha spin ($E_{\alpha-H-L}$) of $Au_n^-$ ($n$ = 7−20) clusters at the PBE0/SDD level of theory. **d,** DFT-calculated electron affinity of the anionic $Au_n^-$ ($n$ = 7−20) clusters, defined by EA = $E(Au_n^-) - E(Au_n^{2-})$ at the optimized $Au_n^-$ geometry.

**Supplementary Table 1 | $Au_nO_2^-$. The NPA charges (Q, in |e|) and spin density populations** ($\mu$, in $\mu_B$) of $Au_nO_2^-$ ($n$ = 7−20) complexes.

| size | $Q_{O_2}$ | $\mu_{O_2}$ | $\mu_{total}$ |
|---|---|---|---|
| 7 | −0.54 | 1 | 2 |
| 8 | −0.47 | 1 | 1 |
| 9 | −0.30 | 1.5 | 2 |
| 10 | −0.31 | 1 | 1 |
| 11 | −0.52 | 1.1 | 2 |
| 12 | −0.58 | 1 | 1 |
| 13 | −0.27 | 1.6 | 2 |
| 14 | −0.58 | 1 | 1 |
| 15 | −0.33 | 1.5 | 2 |
| 16 | −0.55 | 1 | 1 |
| 17 | −0.14 | 1.7 | 2 |
| 18 | −0.51 | 1 | 1 |
| 19 | −0.78 | 0 | 0 |
| 20 | −0.51 | 1 | 1 |

**Supplementary Table 2 | $Au_nNO^-$. The NPA charges (Q, in |e|) and spin density populations** ($\mu$, in $\mu_B$) of $Au_nNO^-$ ($n$ = 7−20) complexes.

| size | $Q_N$ | $Q_O$ | $Q_{NO}$ | $\mu_{NO}$ | $\mu_{total}$ |
|---|---|---|---|---|---|
| 7 | 0 | −0.23 | −0.23 | 0.81 | 1 |
| 8 | −0.1 | −0.26 | −0.36 | 1.33 | 2 |
| 9 | 0.01 | −0.22 | −0.21 | 0.75 | 1 |
| 10 | 0.01 | −0.21 | −0.2 | 0 | 0 |
| 11 | 0.02 | −0.20 | −0.18 | 0.79 | 1 |
| 12 | −0.19 | −0.25 | −0.44 | 1.41 | 2 |
| 13 | −0.01 | −0.22 | −0.23 | 0.93 | 1 |
| 14 | −0.16 | −0.25 | −0.41 | 0 | 0 |
| 15 | −0.02 | −0.23 | −0.25 | 0.88 | 1 |
| 16 | 0.09 | −0.18 | −0.09 | 0 | 0 |
| 17 | 0.04 | −0.19 | −0.15 | 0.85 | 1 |
| 18 | −0.03 | −0.23 | −0.26 | 1.32 | 2 |
| 19 | 0.00 | −0.20 | −0.2 | 0.95 | 1 |
| 20 | −0.09 | −0.25 | −0.34 | 1.36 | 2 |

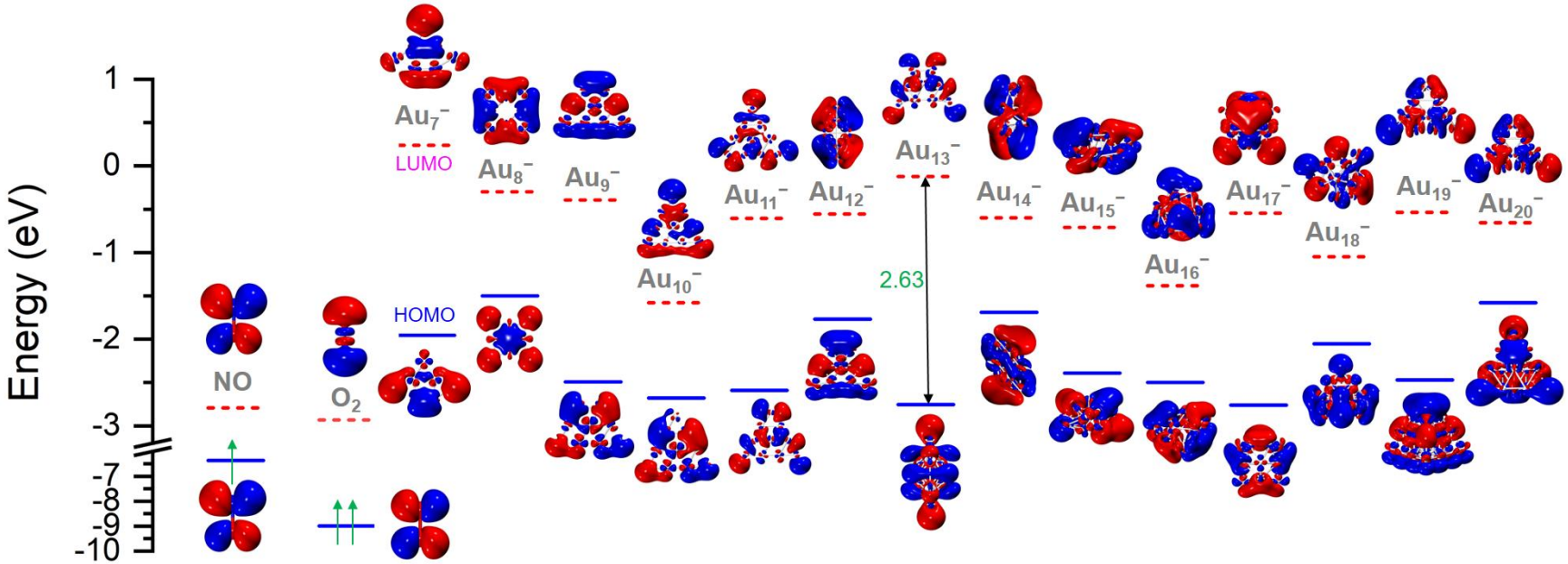
**Supplementary Table 3 | The geometric and electronic properties of $M_n^-$** (M = Cu, Ag, Au; $n$ = 6, 13, 17) clusters under revTPSS/SDD scheme, including average M-M bond length (BL, in Å), total bond number (BN), average coordination number (CN), average Wiberg bond order (BO), and alpha HOMO-LUMO gap ($E_{\alpha\text{-H-L}}$, in eV).

| Cluster | BL | BN | CN | BO | $E_{\alpha\text{-H-L}}$ |
|---|---|---|---|---|---|
| $Cu_6^-$ | 2.40 | 12 | 4 | 0.61 | 1.26 |
| $Ag_6^-$ | 2.76 | 12 | 4 | 0.55 | 1.19 |
| $Au_6^-$ | 2.71 | 9 | 3 | 0.76 | 0.47 |
| $Cu_{13}^-$ | 2.42 | 34 | 5.23 | 0.47 | 1.25 |
| $Ag_{13}^-$ | 2.77 | 34 | 5.23 | 0.42 | 1.31 |
| $Au_{13}^-$ | 2.80 | 33 | 5.08 | 0.53 | 1.52 |
| $Cu_{17}^-$ | 2.50 | 58 | 6.82 | 0.39 | 0.74 |
| $Ag_{17}^-$ | 2.78 | 48 | 5.65 | 0.38 | 1.09 |
| $Au_{17}^-$ | 2.77 | 45 | 5.29 | 0.51 | 1.25 |

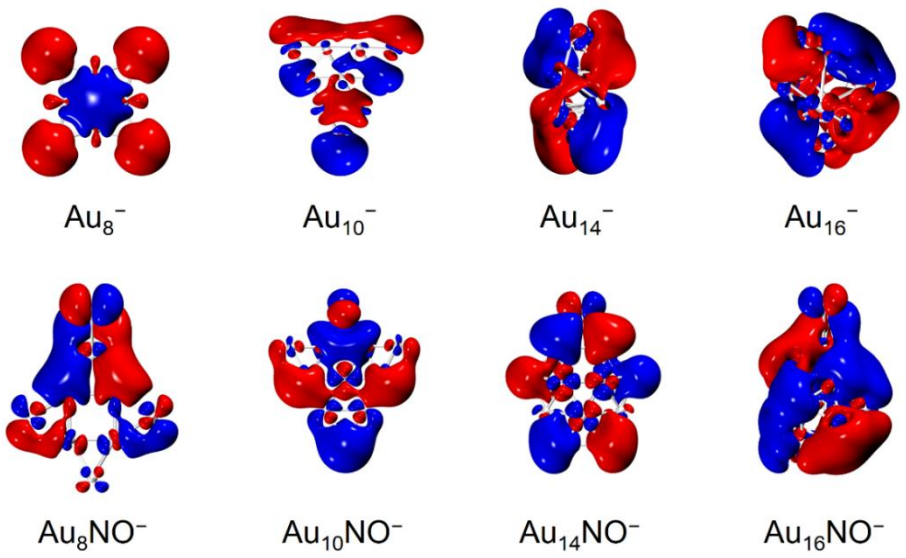
**Supplementary Table 4 | The geometric and electronic properties of $Au_n^-$ ($n$ = 7−20) clusters** under revTPSS/SDD scheme, including average Au-Au bond length (BL, in Å), total bond number (BN), average coordination number (CN), average Wiberg bond order (BO), electron affinity (EA, in eV), vertical electron detachment energies (VDE, in eV), HOMO-LUMO gaps ($E_{H-L}$, in eV) and that under PBE0/SDD scheme ($E_{H-L-PBE0}$, in eV), as well as alpha HOMO-LUMO gaps under PBE0/SDD scheme ($E_{\alpha-H-L-PBE0}$, in eV) for comparison.

| Size | BL | BN | CN | BO | EA | VDE | $E_{H-L}$ | $E_{H-L-PBE0}$ | $E_{\alpha-H-L-PBE0}$ |
|---|---|---|---|---|---|---|---|---|---|
| 7 | **2.68** | 10 | 2.86 | **0.79** | −1.24 | 3.36 | 1.25 | 2.19 | 2.19 |
| 8 | **2.68** | 12 | 3.00 | 0.74 | −0.59 | 2.80 | 0.28 | 1.20 | 1.94 |
| 9 | 2.73 | 16 | 3.56 | 0.68 | −0.56 | 3.68 | 0.99 | 2.10 | 2.10 |
| 10 | 2.72 | 18 | 3.60 | 0.67 | **0.48** | **3.99** | 0.08 | 1.10 | **2.98** |
| 11 | 2.73 | 21 | 3.82 | 0.65 | −0.82 | 3.62 | 1.06 | 1.98 | 1.98 |
| 12 | 2.80 | 30 | 5.00 | 0.53 | −0.35 | 2.99 | 0.23 | 1.21 | 1.74 |
| 13 | 2.80 | 33 | 5.08 | 0.53 | −4.16 | **3.84** | **1.52** | **2.63** | **2.63** |
| 14 | 2.83 | 40 | 5.71 | 0.48 | −0.38 | 2.88 | 0.18 | 1.09 | 1.09 |
| 15 | 2.83 | 43 | 5.73 | 0.48 | −0.20 | 3.50 | 0.71 | 1.68 | 1.68 |
| 16 | 2.78 | 42 | 5.25 | 0.51 | **0.43** | 3.63 | 0.14 | 1.11 | 2.02 |
| 17 | 2.77 | 45 | 5.29 | 0.51 | −0.29 | **3.88** | 1.25 | 2.22 | 2.22 |
| 18 | 2.84 | **58** | **6.44** | 0.43 | **0.15** | 3.22 | 0.13 | 1.01 | 1.65 |
| 19 | 2.82 | 57 | 6.00 | 0.47 | −0.21 | 3.55 | 1.04 | 1.93 | 1.93 |
| 20 | 2.82 | 60 | 6.00 | 0.46 | −0.06 | 2.69 | 0.17 | 0.92 | 0.92 |

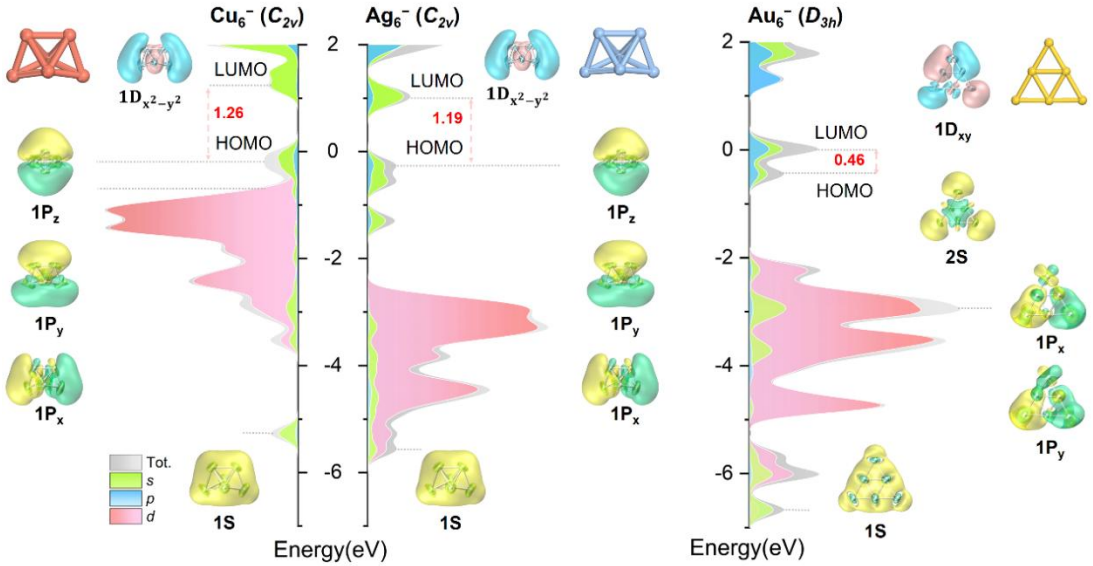
# DOSs and frontier orbitals



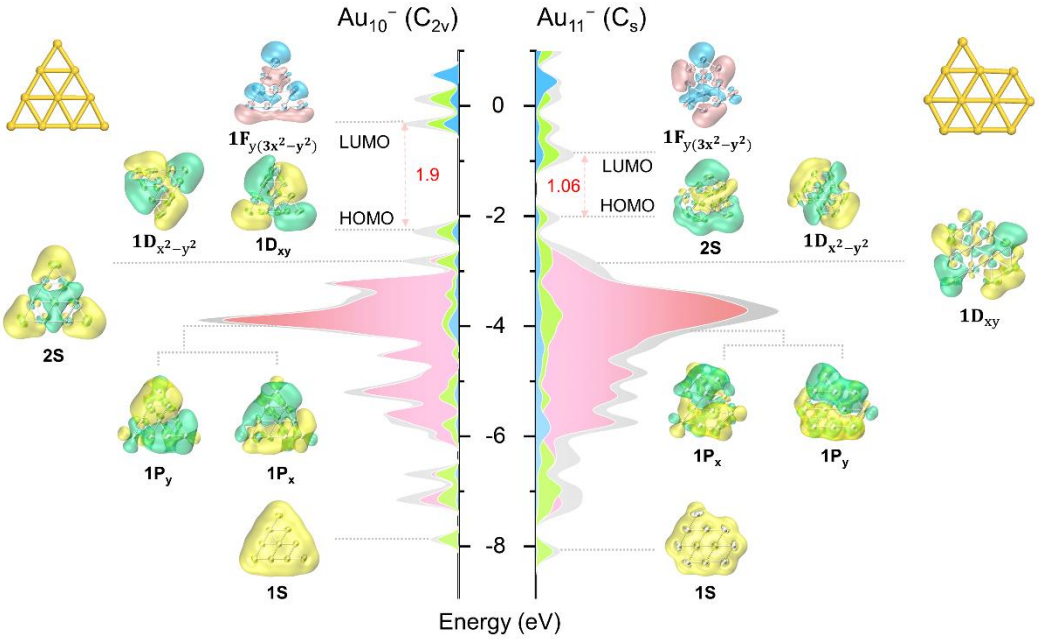

**Supplementary Fig. 14 | Frontier orbital. Energies and electron cloud patterns of the HOMOs and LUMOs of $Au_n^-$** ($n$ = 7−20) clusters and $NO/O_2$ molecules, calculated at the PBE0/SDD level of theory.



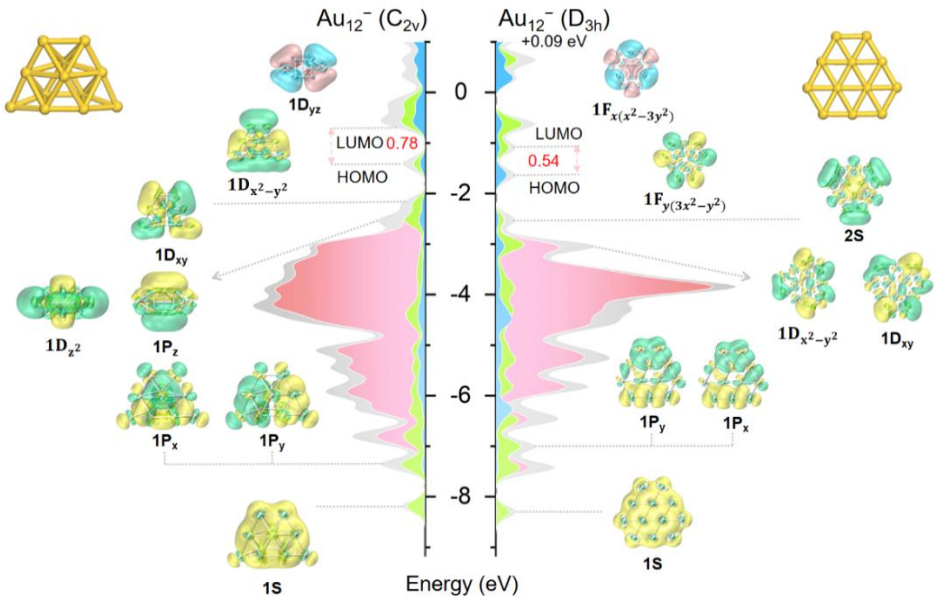

**Supplementary Fig. 15 | A comparison of even-numbered $Au_n^-$ clusters**. The electron cloud pattern of the HOMOs of typical $Au_{2n}^-$ clusters and $Au_{2n}NO^-$ complexes.



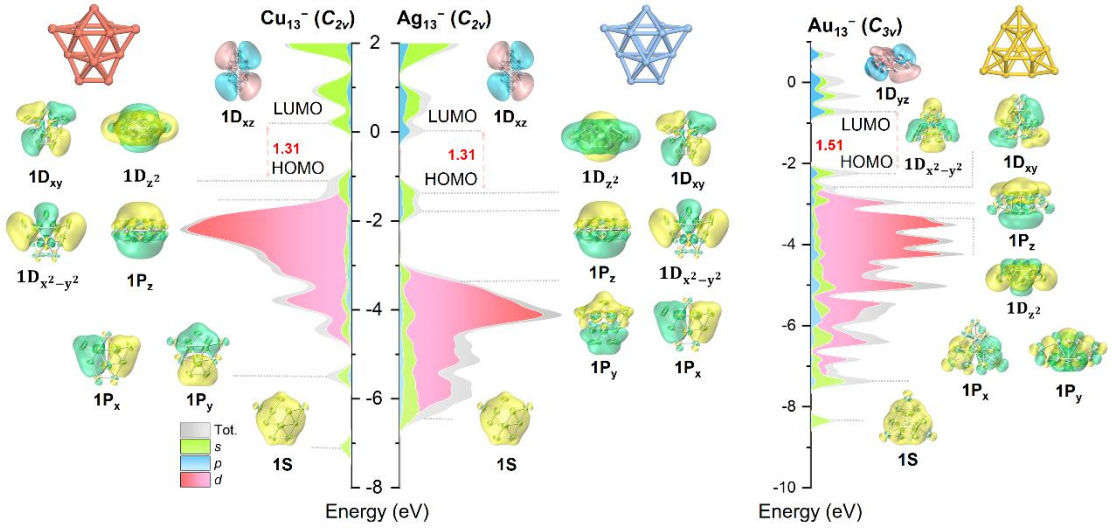

**Supplementary Fig. 16 | DOS analysis of $Cu_6^-$, $Ag_6^-$ and $Au_6^-$.** Partial densities of states (PDOS), energy levels and superatomic orbitals for $M_6^-$ (M = Cu, Ag, Au) clusters. The results are calculated at the revTPSS/SDD level of theory. The light grey shaded area donates the total density of states (TDOS), whereas the red, blue and green curves represent the PDOS contributions from the M *s*, *p*, and *d* orbitals, respectively. Unless otherwise noted, an isovalue of 0.01 a.u. is used throughout this work. For the orbital patterns, yellow and green patterns denote the positive and negative phases of the wavefunctions, respectively, while pink and blue denote the positive and negative phases of the LUMO wavefunction, respectively.



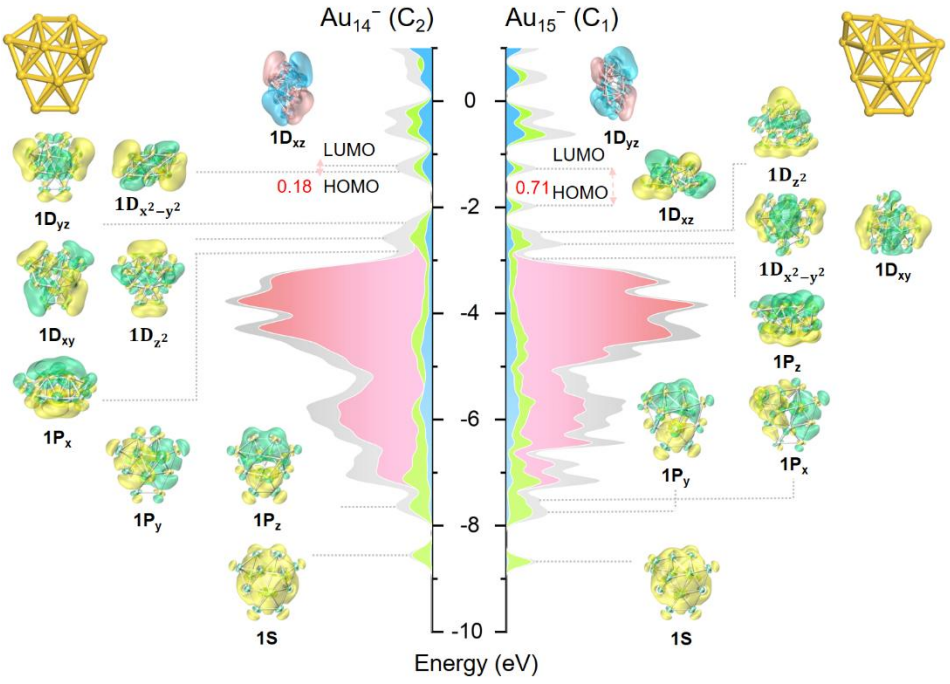

**Supplementary Fig. 17 | DOS analysis of $Au_{10}^-$ and $Au_{11}^-$.** PDOS, energy levels and superatomic orbitals for $Au_{10}^-$ and $Au_{11}^-$ clusters. The results are calculated at the revTPSS/SDD level of theory.



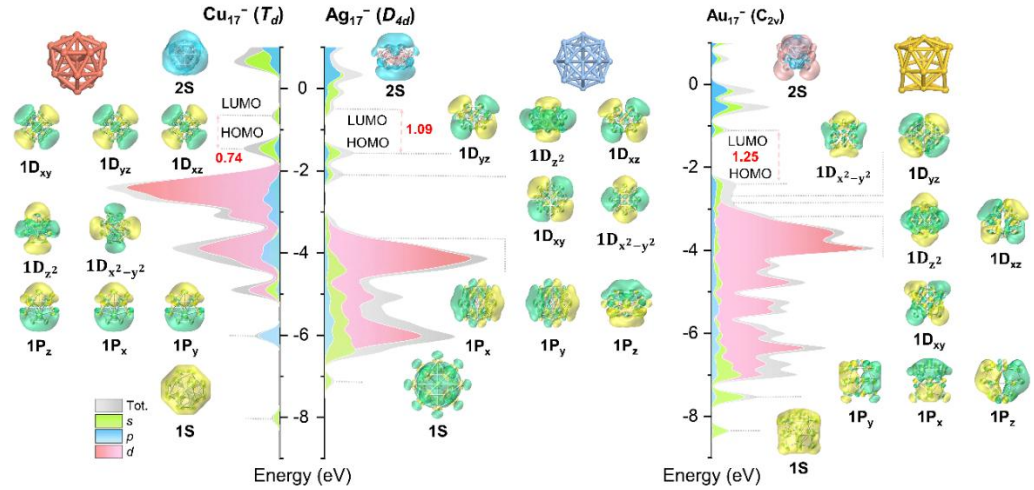

**Supplementary Fig. 18 | DOS analysis of low-lying $Au_{12}^-$ isomers**. PDOS, energy levels and superatomic orbitals for $Au_{10}^-$ and $Au_{11}^-$ clusters. The results are calculated at the revTPSS/SDD level of theory.



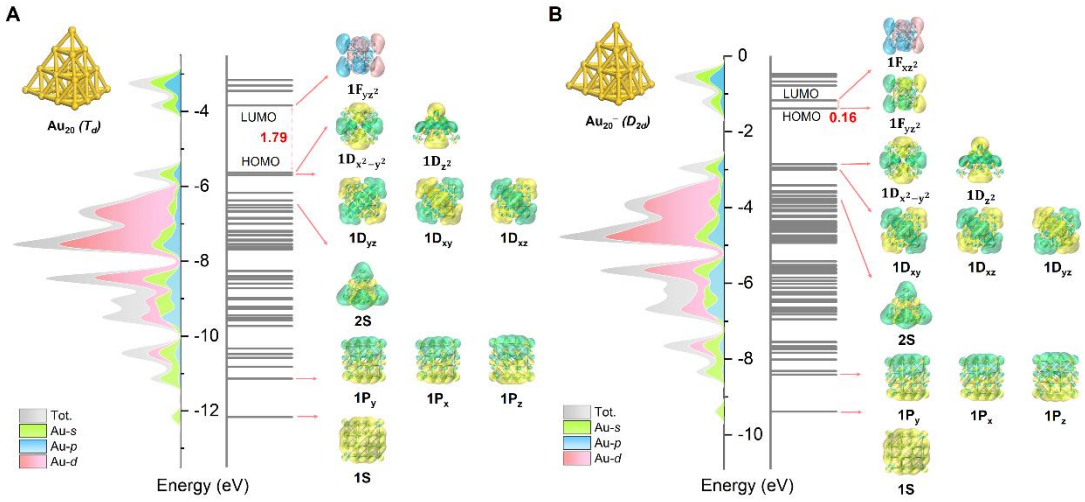

**Supplementary Fig. 19 | DOS analysis of $Cu_{13}^-$, $Ag_{13}^-$ and $Au_{13}^-$.** PDOS, energy levels and superatomic orbitals for $M_{13}^-$ (M = Cu, Ag, Au) clusters. The results are calculated at the revTPSS/SDD level of theory. The *a/c* ratios of $Cu_{13}^-$, $Ag_{13}^-$, and $Au_{13}^-$ clusters are 1.53, 1.61 and 1.60, respectively.



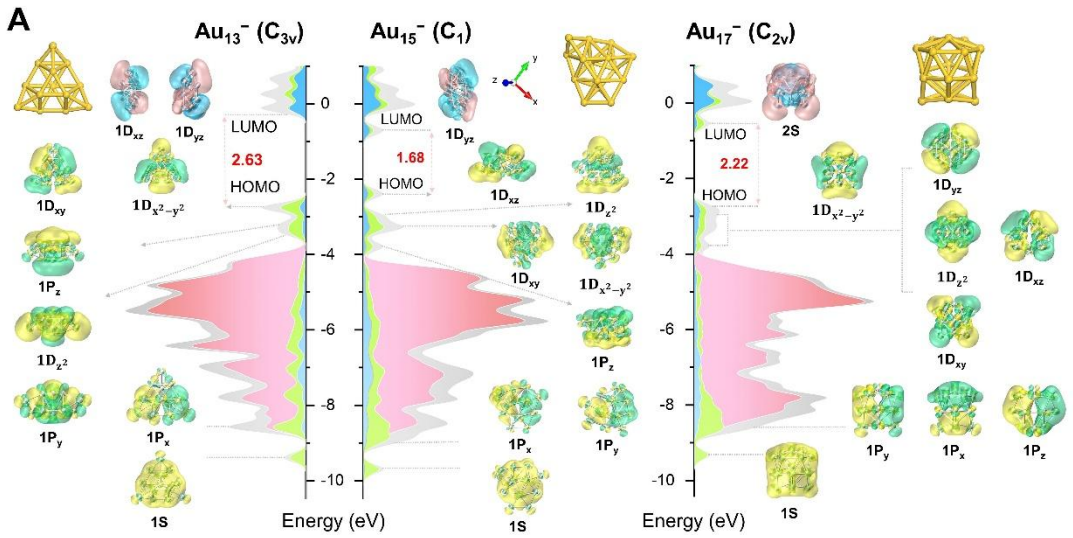

**Supplementary Fig. 20 | DOS analysis of $Au_{14}^-$ and $Au_{15}^-$.** PDOS, energy levels and superatomic orbitals for $Au_{10}^-$ and $Au_{11}^-$ clusters. The results are calculated at the revTPSS/SDD level of theory.



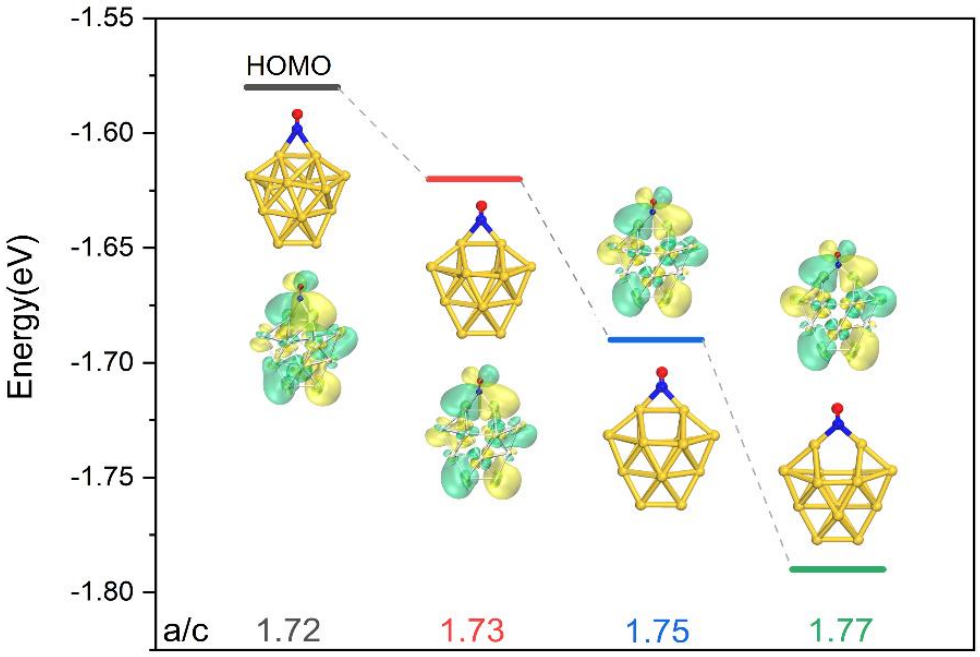

**Supplementary Fig. 21 | DOS analysis of $Cu_{17}^-$, $Ag_{17}^-$ and $Au_{17}^-$.** PDOS, energy levels and superatomic orbitals for $M_{17}^-$ (M = Cu, Ag, Au) clusters. The results are calculated at the revTPSS/SDD level of theory. The *a*/*c* ratios of $Cu_{17}^-$, $Ag_{17}^-$, and $Au_{17}^-$ clusters are 1, 1.28 and 1.01, respectively.



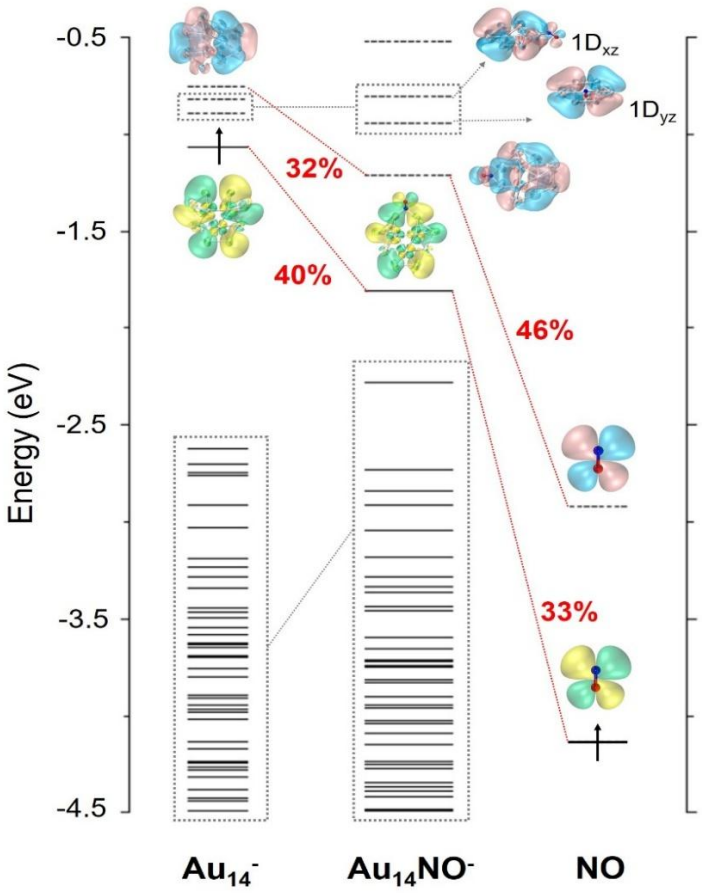

**Supplementary Fig. 22 | DOS analysis of $Au_{20}^-$ and $Au_{20}$.** PDOS, energy levels and superatomic orbitals for the $Au_{20}^-$ cluster and its neutral counterpart $Au_{20}$. The results are calculated at the revTPSS/SDD level of theory. $Au_{20}^-$ disrupts the 20e closed-shell configuration of the $Au_{20}$ cluster, and consequently its symmetry is reduced to $D_{2d}$ due to the Jahn–Teller effect.



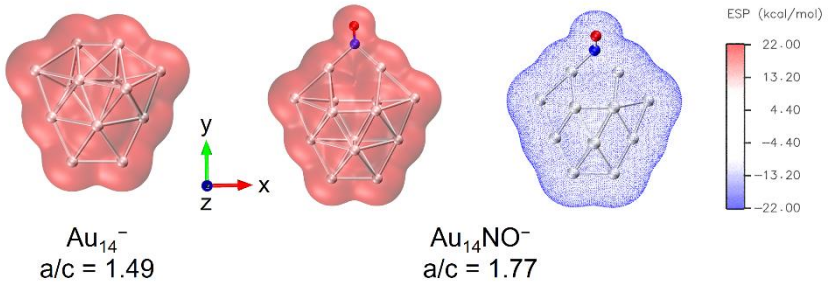

**Supplementary Fig. 23 | PDOS and energy levels at hybrid functional.** Superatomic orbitals for the $Au_{13}^-$, $Au_{15}^-$, and $Au_{17}^-$ clusters, calculated at the PBE0/SDD level of theory.



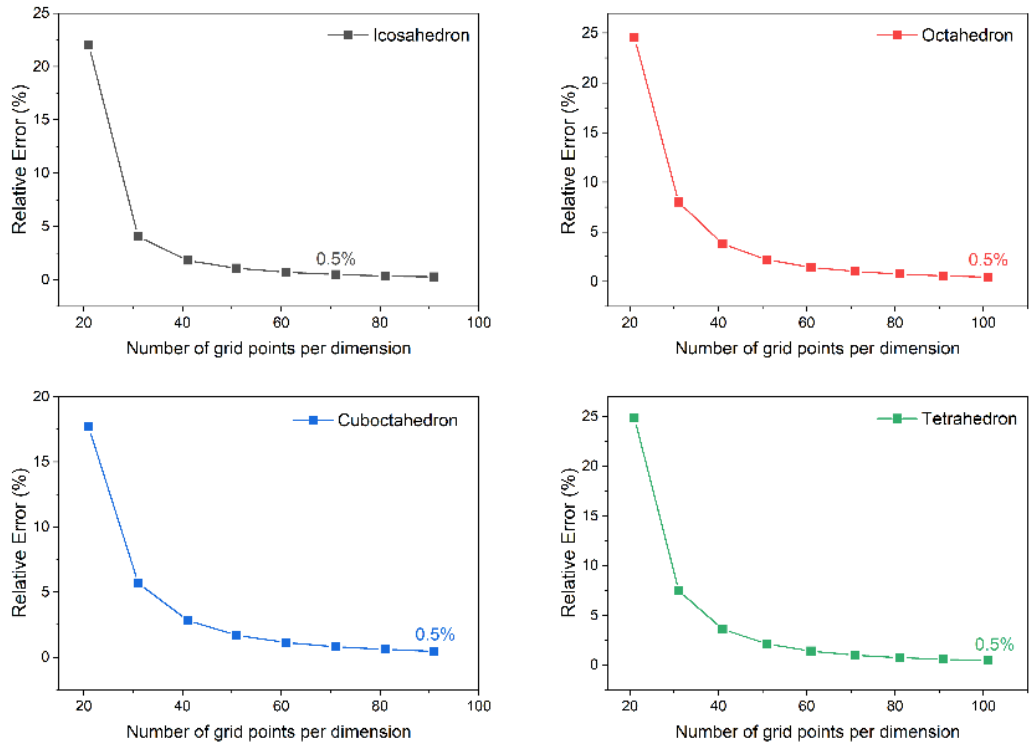

**Supplementary Fig. 24 | HOMO energy level in $Au_{14}NO^-$ sensitive to the *a/c* ratio,** along with the electron cloud pattern during its formation process, calculated at the revTPSS/SDD level of theory.



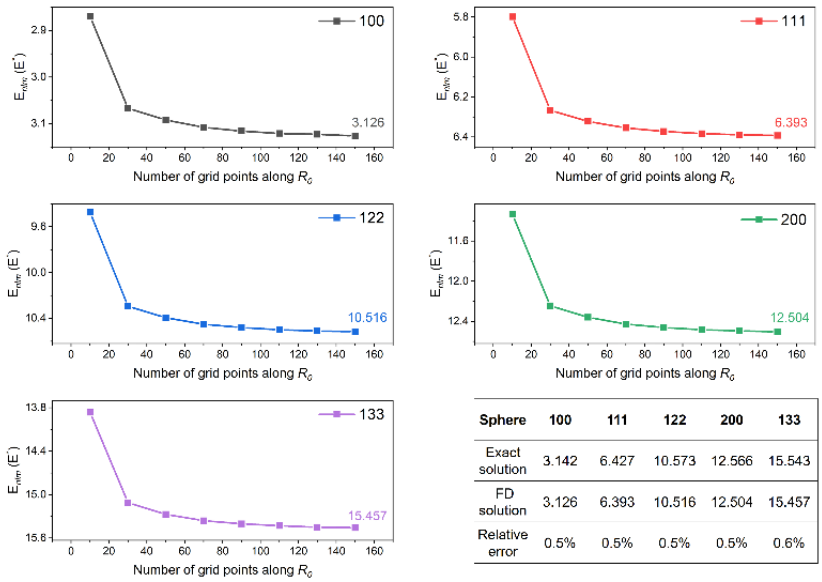

**Supplementary Fig. 25 | Charge decomposition analysis (CDA).** The correlation between the energy levels of the $Au_{14}NO^-$ cluster and its constituent fragments ($Au_{14}^-$ and NO), shown from −4.5 eV to −0.5 eV. Gray lines trace orbital correlations with a fragment contribution of at least 10%, while red lines highlight strong mutual contributions (>10% each). Insets depict the electron cloud distributions of key molecular orbitals.




**Supplementary Fig. 26 | Electron density surfaces (red) and electrostatic potential surfaces** (blue isosurface) of $Au_{14}^-$ cluster and $Au_{14}NO^-$ complex, calculated at the revTPSS/SDD level of theory.



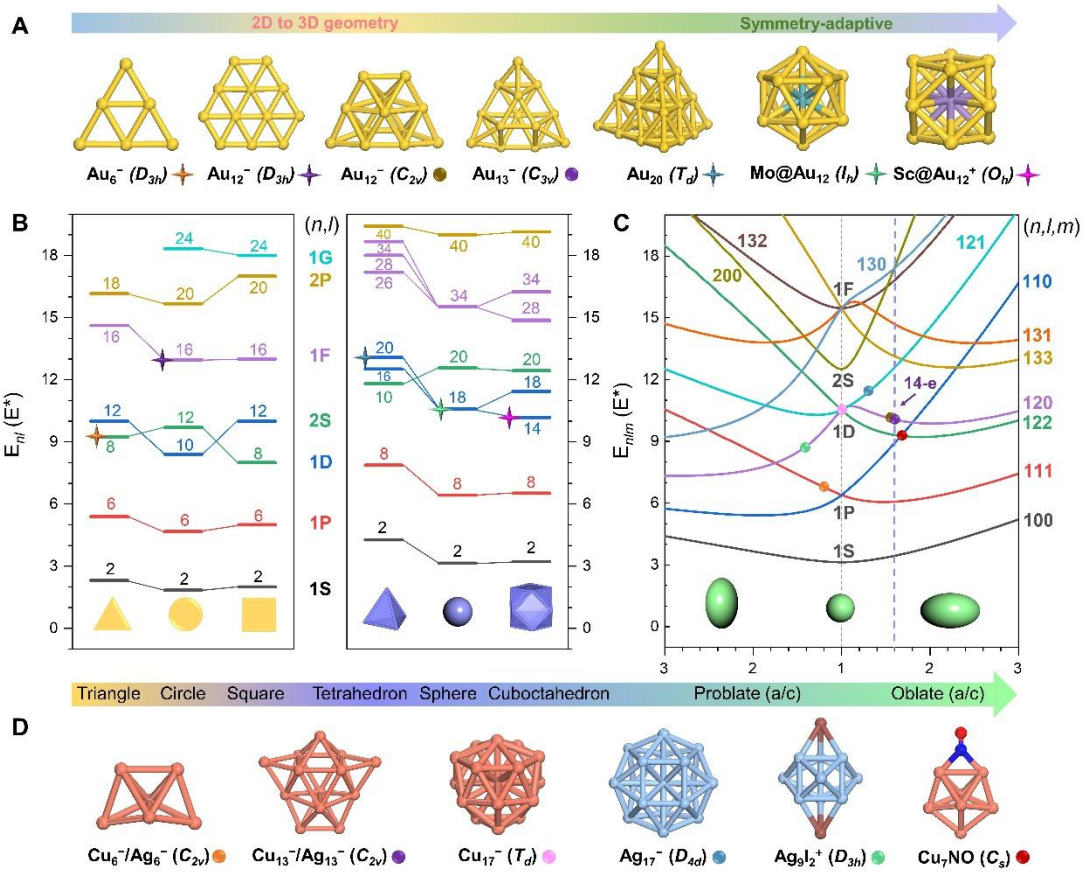

**Supplementary Fig. 27 | Grid convergence test for the four polyhedral wells:** icosahedron, octahedron, cuboctahedron, and tetrahedron. The horizontal axis denotes the number of grid points per dimension ($N_{grid}$). For each $N_{grid}$, the vertical axis shows the relative change (in percent) of the lowest 5 non-degenerate eigenvalues compared to the previous thicker grid, calculated as $\frac{\left|E(N_{grid,prev})-E(N_{grid})\right|}{E(N_{grid,prev})} \times 100\%$ and averaged over the 5 states. The smallest $N_{grid}$ that satisfies the convergence threshold (0.5%) is chosen for the production calculations. These values are: $N_{grid} = 71$ (icosahedron), $N_{grid} = 101$ (octahedron), $N_{grid} = 91$ (cuboctahedron), and $N_{grid} = 101$ (tetrahedron).




| Sphere | 100 | 111 | 122 | 200 | 133 |
|---|---|---|---|---|---|
| Exact solution | 3.142 | 6.427 | 10.573 | 12.566 | 15.543 |
| FD solution | 3.126 | 6.393 | 10.516 | 12.504 | 15.457 |
| Relative error | 0.5% | 0.5% | 0.5% | 0.5% | 0.6% |

**Supplementary Fig. 28 | Benchmark grid points test of three-dimensional infinite spherical potential well**, with potential energy calculated on the finite difference (FD) method and exact solution. The results show that when the number of grid points is 150, the error ($\frac{|E_{exact}-E_{FD}|}{E_{exact}} \times 100\%$) of the FD method is ~0.5% relative to solution value.

Although $Au_{10}^-$ has a 2D geometry, its electron-density surface corresponds to 3D patterns. GCSS calculations indicate that superatomic orbital components along the short-axis (*z*-axis) direction are present, though they occur at relatively high unoccupied energy levels. As shown in Supplementary Fig. 29, the 2D triangular, circular, and square structures display closed shell structures when the valence electron counts reach 2, 6, 12, and 16—values that correspond to electronic magic numbers. Upon reaching the six electron (6e) closed-shell arrangement, a 2D-to-3D structural transition becomes possible, driven by the large energy gaps between the 6e shell and the 1D or 2S levels, along with a tendency to enhance cluster stability by increasing bond strength but with fewer chemical bonds or decreasing bond strength with more chemical bonds. This is reasonable for $Cu_n^-$ and $Ag_n^-$ clusters which undergo a transition to 3D structures at $n = 6$. In contrast, due to strong relativistic effects and pronounced *s-d* hybridization, $Au_n^-$ clusters can enhance stability by forming only a small number of additional chemical bonds (Supplementary Tables 3 and 4), thereby maintaining their 2D structure until $n = 12$. The larger gold clusters with $n \geq 12$ require additional electrons to attain a 1F closed-shell configuration (Supplementary Fig. 29).



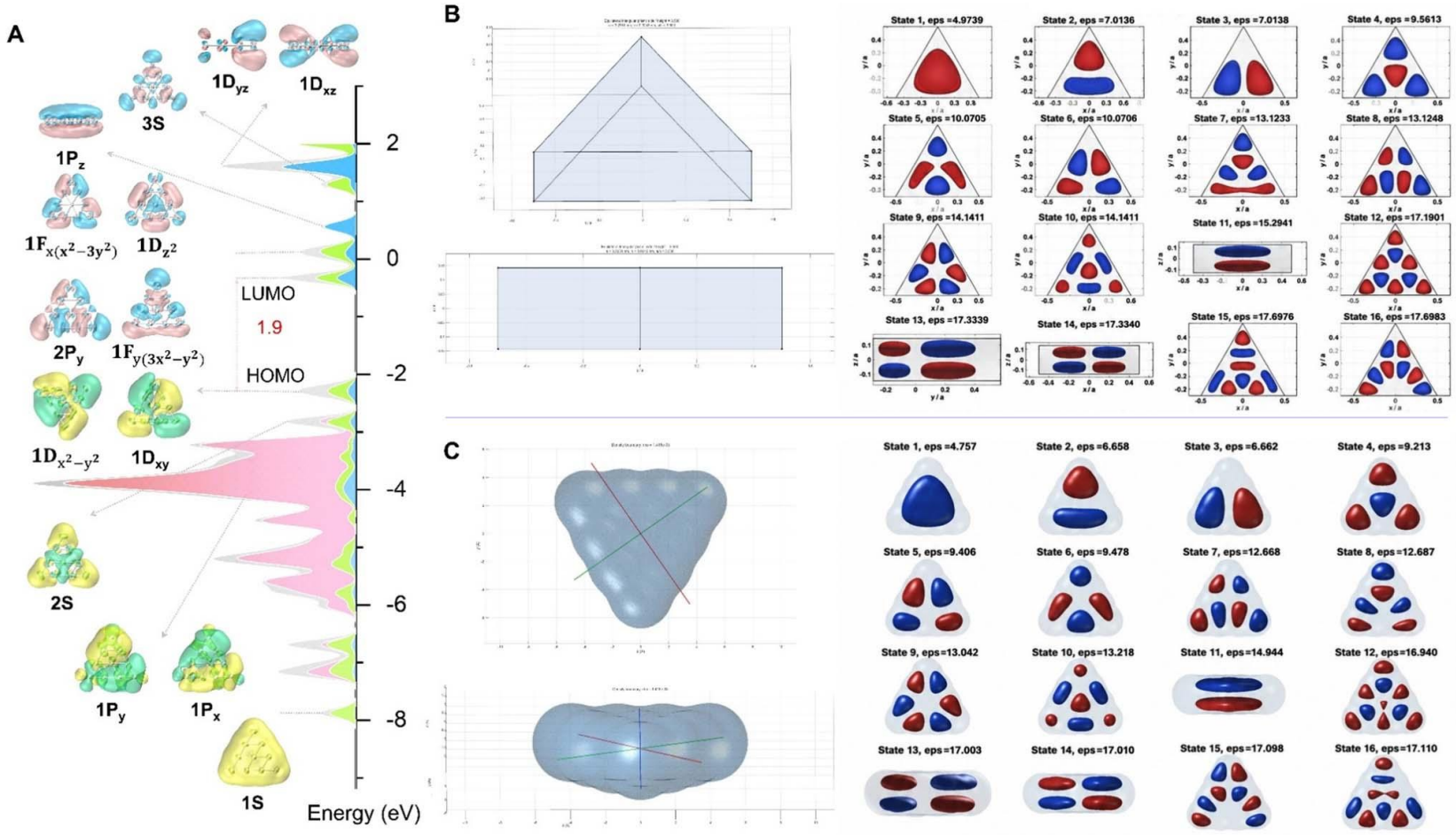

**Supplementary Fig. 29 | Coinage metal clusters in GCSS model. A,** Structures and symmetries of typical pure and single-atom-doped gold clusters. **B,** Energy-level diagrams of 2D infinite-well potentials with triangular, circular, and square symmetries **(**Left**)** and **e**nergy-level diagrams of 3D infinite-well potentials with tetrahedral, spherical, and cuboctahedral symmetries **(**Right**)**. **C,** Influence of well shape on the energy levels as a function of prolate/oblate ellipsoidal distortion. **D,** Structures and symmetries of typical pure and ligand-modified copper/silver clusters.

This GCSS model can be applicable to oblate systems. A 3D oblate ellipsoidal structure denotes a 14e shell structure corresponding to a 1D subshell closure for $Au_{13}^-$ ($1S^2|1P^4|1P^2|1D^6||1D^0|$). Both the Clemenger-Nilsson ellipsoidal model and our GCSS model calculations show that, at this axial *a/c* ratio, the energy gap due to the splitting of one-dimensional levels with magnetic quantum numbers $m$ = 1 or 0 surpasses the orbital gap between the superatomic 1D and 2S states under a spherical potential. This feature endows good energetic stability to $Au_{13}^-$, which is also applicable to $Ag_{13}^-$ and $Cu_{13}^-$. It should be highlighted that $Au_{13}^-$ retains greater stability against air exposure than the $Cu_{13}^-$ and $Ag_{13}^-$ counterparts, as copper and silver undergo oxidation far more readily[74].

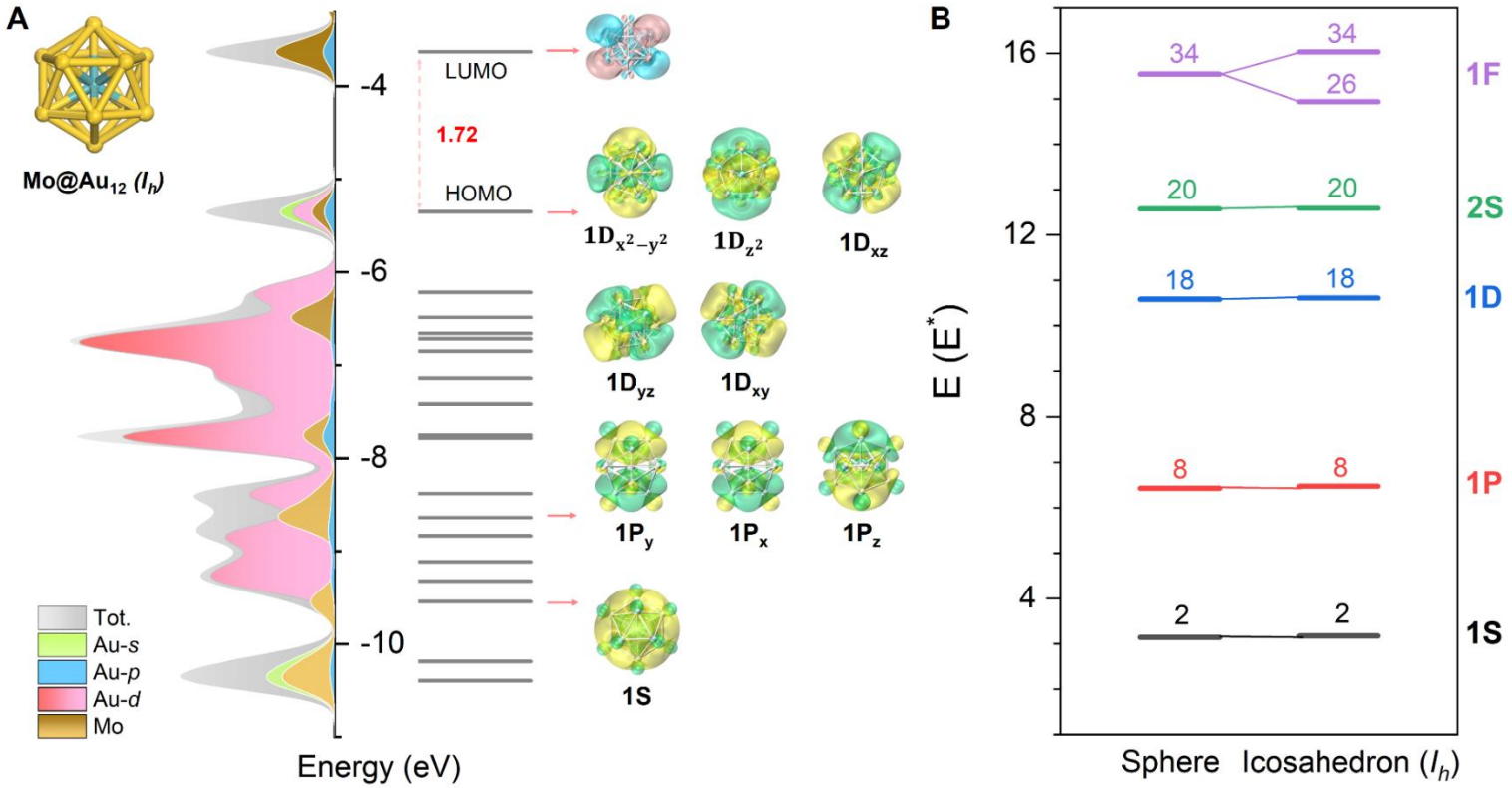
Increasing the axial ratio *a/c* gradually amplifies the energy splitting between the 1P and 1D states. At *a/c* = 1.67, the 1P and 1D levels start to cross and subsequently undergo orbital mixing. Meanwhile, partial 1F levels gradually shift toward lower energy; at the same ratio of 1.67, the 1D and 1F levels cross and mix with one another. Analysis of electron density surface yields deformation ratios (a*/c* of the arbitrary potential domain Ω) of 1.49 for $Au_{14}^-$ and 1.77 for $Au_{14}NO^-$ (more details in Supplementary Fig. 23). At *a/c* = 1.77, this cluster with 16 valence electrons adopts a closed subshell configuration ($1S^2|1P^4|1P^21D^2|1D^4|1F^2||$), which matches perfectly with the superatomic orbital energy ordering of $Au_{14}NO^-$ as DFT results.

Under a triangular potential field, a considerable gap exists between the 1D and 1F energy levels, which corresponds to the $Au_{10}^-$ cluster with the globally largest alpha HOMO-LUMO gap (Supplementary Figs. 17 and 30, Supplementary Table 4). With increasing atomicity, $Cu_{17}^-$, $Ag_{17}^-$, and $Au_{17}^-$ adopt core-shell structures, featuring closed geometric shell structures and prominent 18e stability (Supplementary Fig. 21). Beyond the geometric and electronic shell closure of $Au_{17}^-$, the highly symmetric potential field of the tetrahedral packing configuration further result in reasonable 20e stability of $Au_{20}$ (Supplementary Fig. 22)[75]. Also, the relative stability of the lower-symmetry $Au_{15}^-$ (Supplementary Fig. 20) can be interpreted within a 16e shell stems from the splitting of the 1D level within an asymmetric potential well.

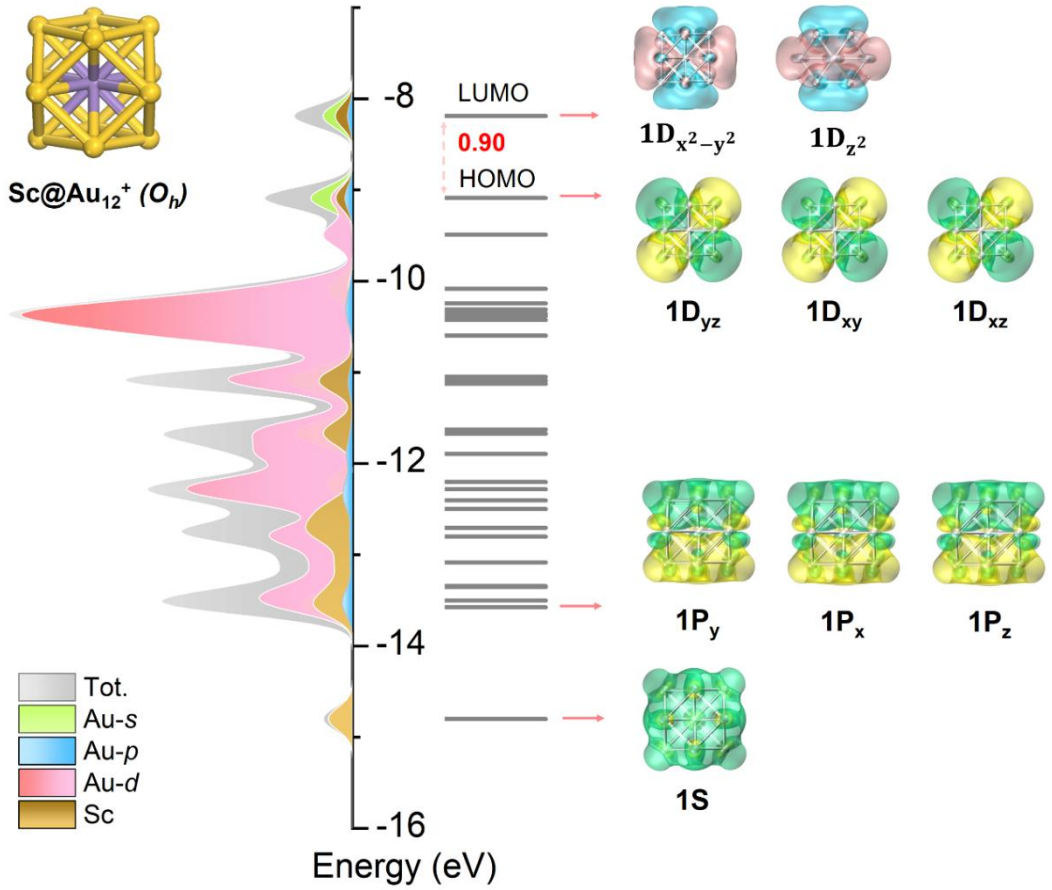
Further, the construction of stable clusters can be modulated through heteroatom doping or ligand passivation[76]. For instance, the doped $Mo@Au_{12}$ cluster features an icosahedral ($I_h$) geometry, which forms an 18e superatom with a closed-shell electronic arrangement. This characteristic arises from rational orbital splitting within the $I_h$ potential field (Supplementary Fig. 31). Such structural symmetry is also valid for other $M@Au_{12}$ clusters[60], as well as ligand-stabilized $Au_{13}$ nanoclusters[77-86]. By contrast, gold clusters confined to a cuboctahedral potential field can attain a closed-shell configuration with merely 14 valence electrons, as exemplified by $Sc@Au_{12}^+$ that possesses an $O_h$ symmetry (Supplementary Fig. 32)[60,87]. These findings demonstrate that the atomic structures of subnanometer metal clusters can be regulated via heteroatom doping.



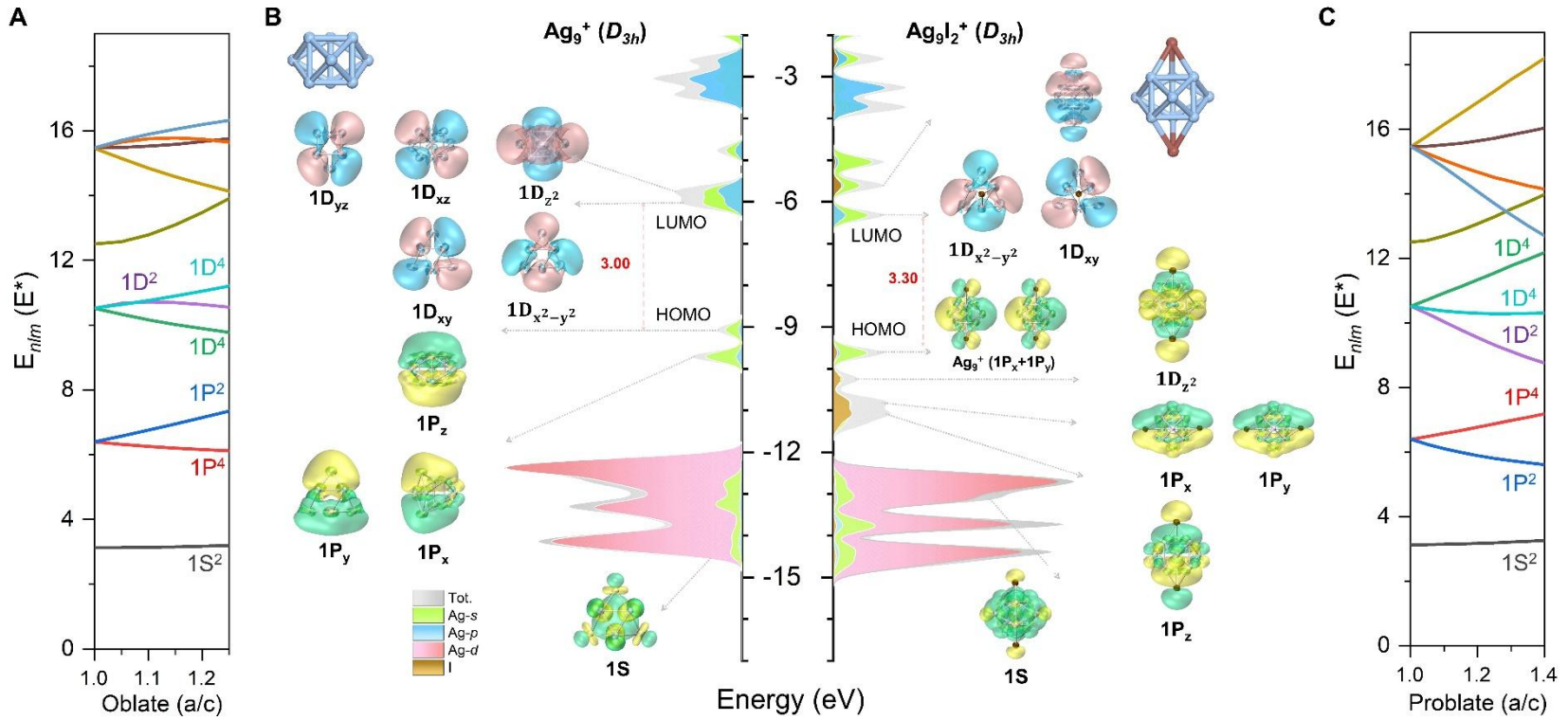

**Supplementary Fig. 30 | Orbital patterns obtained with different methods. A**, DOS, energy levels, and superatomic orbitals of the $Au_{10}^-$ cluster, calculated at the revTPSS/SDD level. **B**, Energy levels and orbital patterns within the GCSS model for a triangular prism with a length-to-height ratio of 3.5. **C**, DFT-calculated electron-density isosurface at an isovalue of 0.0014 a.u.



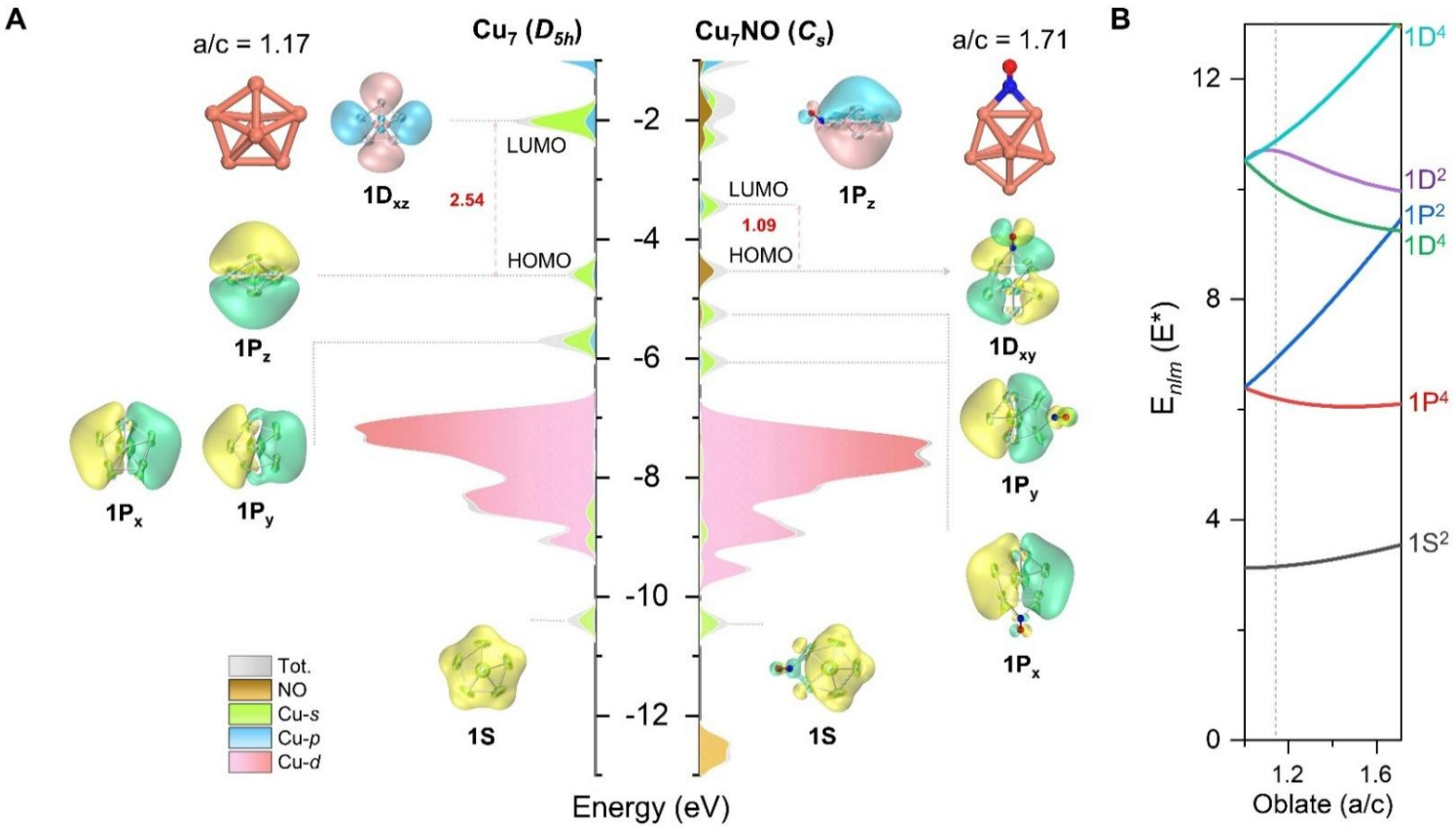

**Supplementary Fig. 31 | DOS analysis of Mo@Au12. A**, PDOS, energy levels and superatomic orbitals for Mo@Au12 cluster. The results are calculated at the revTPSS/SDD level of theory. **B**, Energy-level diagrams of 3D infinite-well potentials within spherical (left) and icosahedral (right) symmetries.




**Supplementary Fig. 32 | DOS analysis of $Sc@Au_{12}^{+}$.** PDOS, orbital energy levels of the $Sc@Au_{12}^{+}$ cluster. The insets show the cluster structure and typical α-orbitals with superatom features. The results are calculated at the revTPSS/SDD level of theory.




**Supplementary Fig. 33 | Orbital patterns of $Ag_9^+$ vs. $Ag_9I_2^+$. A**, Energy-level evolution of the frontier superatomic orbitals as a function of *a/c* within the oblate shell model. The *a/c* range is cut off at 1.25, corresponding to the $Au_9^+$ structure. **B**, PDOS, energy levels and superatomic orbitals for $Ag_9^+$ and $Ag_9I_2^+$ clusters. The results are calculated at the PBE0/SDD level of theory. **C**, Energy-level evolution of the frontier superatomic orbitals as a function of *a/c* within the problate shell model. The *a/c* range is cut off at 1.4, corresponding to the $Au_9I_2^+$ structure.




**Supplementary Fig. 34 | Orbital patterns of $Cu_7$ vs. $Cu_7NO$. A**, PDOS, energy levels and superatomic orbitals for neutral $Cu_7$ and $Cu_7NO$ clusters. The insets show the cluster structures and typical α-orbitals with superatom features, calculated at the PBE0/SDD level of theory. **B**, Energy-level evolution of the frontier superatomic orbitals as a function of *a/c* within the oblate shell model. The *a/c* range is cut off at 1.7, which corresponds to the $Cu_7NO$ structure; the dashed line at *a/c* = 1.17 refers to the $Cu_7$ structure.

**Supplementary Table 5 | GCSS-computed results for oblate metal clusters** using DFT electron-density surfaces as confinement boundaries, in comparison to DFT calculations at the revTPSS/SDD level of theory.

| Cluster | E_GCSS (E*) | | | | | | E_DFT (eV) | | | | | |
|---|---|---|---|---|---|---|---|---|---|---|---|---|
| $Na_7^-$ | 1S(100) | 1P(111) | 1P(110) | | | | 1S | $1P_{x, y}$ | $1P_z$ | | | |
| | 3.14 | 6.18 | 6.85 | | | | -1.58 | -0.35 | 0.1 | | | |
| $Mg_7$ | 1S(100) | 1P(111) | 1P(110) | 1D(122) | 1D(120) | | 1S | $1P_{x, y}$ | $1P_z$ | $1D_{xy, x^2-y^2}$ | $1D_{z^2}$ | |
| | 3.44 | 6.18 | 8.50 | 9.33 | 9.85 | | -8.47 | -6.27 | -5.21 | -4.06 | -4.1 | |
| $[Au_7]^{3-}$ | 1S(100) | 1P(111) | 1D(122) | | | | 1S | $1P_{x, y}$ | $1D_{xy, x^2-y^2}$ | | | |
| | 4.16 | 6.19 | 8.86 | | | | 2.06 | 2.67 | 4.80 | | | |
| $[Au_{12}]^{4-}$ | 1S(100) | 1P(111) | 1D(122) | 1D(120) | 1F(133) | | 1S | $1P_{x, y}$ | $1D_{xy, x^2-y^2}$ | $1D_{z^2}$ | $1F_{x(x^2-3y^2),y(3x^2-y^2)}$ | |
| | 4.96 | 6.76 | 9.20 | 9.78 | 11.72; 12.75 | | -1.66 | -1.24 | 0.13 | 0.49 | 1.49; 1.87 | |
| $Ag_{17}^-$ | 1S(100) | 1P(111) | 1P(110) | 1D(122) | 1D(120) | 1D(121) | 1S | $1P_{x, y}$ | $1P_z$ | $1D_{xy, x^2-y^2}$ | $1D_{z^2}$ | $1D_{xz, yz}$ |
| | 3.17 | 6.17 | 7.07 | 9.94 | 10.76 | 10.86 | -7.11 | -3.58 | -3.23 | -2.09 | -1.58 | -1.57 |

**Supplementary Table 6 | GCSS-computed results for prolate metal clusters** using DFT electron-density surfaces as confinement boundaries, in comparison to DFT calculations at the revTPSS/SDD level of theory.

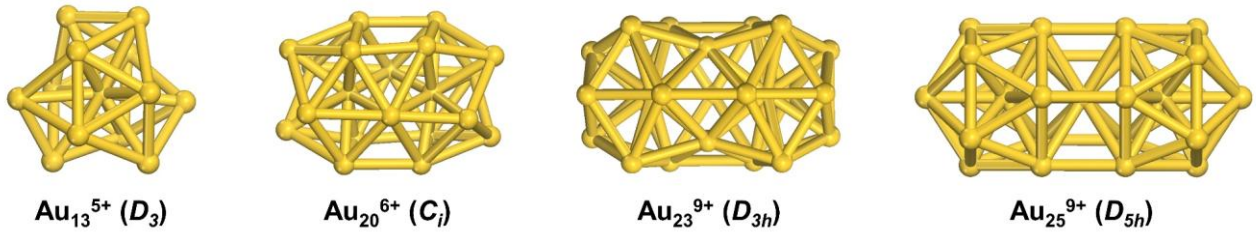
| Cluster | E_GCSS (E*) | | | | | | E_DFT (eV) | | | | | |
|---|---|---|---|---|---|---|---|---|---|---|---|---|
| $[Ag_6]^{2-}$ | 1S(100) | 1P(110) | 1P(111) | | | | 1S | $1P_z$ | $1P_{x,y}$ | | | |
| | 3.18 | 6.44 | 6.45 | | | | -0.27 | 2.69 | 2.70 | | | |
| $Mg_{11}$ | 1S(100) | 1P(110) | 1P(111) | 1D(120) | 1D(121) | 1D(122) | 1S | $1P_z$ | $1P_{x,y}$ | $1D_{z^2}$ | $1D_{xz,yz}$ | $1D_{xy,x^2-y^2}$ |
| | 3.34 | 6.22 | 7.00 | 9.06 | 11.37 | 11.46 | -8.71 | -7.18 | -6.81 | -5.79 | -4.52 | -4.44 |
| | 1F(130) | 2S(200) | | | | | $1F_{z^3}$ | 2S | | | | |
| | 12.30 | 12.77 | | | | | -4.09 | -4.08 | | | | |
| $Ag_9I_2^+$ | 1S(100) | 1P(110) | 1P(111) | 1D(120) | | | 1S | $1P_z$ | $1P_{x,y}$ | $1D_{z^2}$ | | |
| | 3.43 | 6.19 | 7.24 | 8.71 | | | -13.11 | -10.16 | -10.1 | -9.42 | | |
| $[Au_{23}]^{9+}$ | 1S | $1P_z$ | $1P_{x,y}$ | $1D_{z^2}$ | $1D_{xz,yz}$ | | 1S | $1P_z$ | $1P_{x,y}$ | $1D_{z^2}$ | $1D_{xz,yz}$ | |
| | 3.48 | 5.47 | 7.82 | 8.76 | 10.03 | | -35.83 | -35.55 | -33.35 | -33.08 | -32.87 | |
| $Au_3^-$ | 1S(100) | 1P(110) | | | | | 1S | $1P_z$ | | | | |
| | 3.99 | 5.09 | | | | | -2.04 | -1.35 | | | | |
| $[Na_2Cl_2]^{2-}$ | 1S(100) | | | | | | 1S | | | | | |
| | 5.14 | | | | | | 4.06 | | | | | |

**Supplementary Table 7 | GCSS-computed results for metal clusters of triangular prism structure** using DFT electron-density surfaces as confinement boundaries, in comparison to DFT calculations at the revTPSS/SDD level of theory.

| Cluster | E_GCSS (E*) | | | | | | E_DFT (eV) | | | | | |
|---|---|---|---|---|---|---|---|---|---|---|---|---|
| $Sn_6$ | 1S($a_1$') | 1P($a_2$'') | 1P(e') | 1D(e'') | 1D($a_1$') | 2S($a_1$') | 1S($a_1$') | 1P($a_2$'') | 1P(e') | 1D(e'') | 1D($a_1$') | 2S($a_1$') |
| | 3.45 | 6.43 | 6.84;6.94 | 9.76;9.93 | 11.40 | 11.92 | -14.21 | -12.13 | -11.53;-11.76 | -9.19;-9.45 | -6.61 | -6.12 |
| | 1D(e') | | | | | | 1D(e') | | | | | |
| | 12.04;12.12 | | | | | | -5.84;-5.63 | | | | | |
| $Al_3^+$ | 1S($a_1$') | 1P(e') | 1P($a_2$'') | | | | 1S($a_1$') | 1P(e') | 1P($a_2$'') | | | |
| | 3.44 | 5.95 | 8.32 | | | | -16.29 | -12.46 | -9.20 | | | |
| $[Mg_3]^{2-}$ | 1S($a_1$') | 1P(e') | 1P($a_2$'') | | | | 1S($a_1$') | 1P(e') | 1P($a_2$'') | | | |
| | 3.53 | 6.04 | 8.50 | | | | 1.09 | 3.07 | 4.74 | | | |
| $Au_6$ | 1S($a_1$') | 1P(e') | | | | | 1S($a_1$') | 1P(e') | | | | |
| | 3.98 | 6.15 | | | | | -7.35 | -5.91 | | | | |
| $[Au_{10}]^{2-}$ | 1S($a_1$') | 1P(e') | 2S($a_1$') | 1D(e') | | | 1S($a_1$') | 1P(e') | 2S($a_1$') | 1D(e') | | |
| | 4.79 | 6.69 | 9.21 | 9.48 | | | -1.10 | -0.77 | 0.31 | 1.04 | | |

**Supplementary Table 8 | GCSS-computed results for triangular pyramid metal clusters** using DFT electron-density surfaces as confinement boundaries, in comparison to DFT calculations at the revTPSS/SDD level of theory.

| Cluster | E_GCSS (E*) | | | | | E_DFT (eV) | | | | |
|---|---|---|---|---|---|---|---|---|---|---|
| $Na_4$ | $1S(a_1)$ | 1P(e) | | | | $1S(a_1)$ | 1P(e) | | | |
| | 3.33 | 5.53 | | | | -4.28 | -2.20 | | | |
| $Na_{10}$ | $1S(a_1)$ | $1P(a_1)$+1P(e) | $2S(a_1)$ | | | $1S(a_1)$ | $1P(a_1)$+1P(e) | $2S(a_1)$ | | |
| | 3.89 | 7.08 | 10.39 | | | -4.73 | -3.54 | -2.30 | | |
| $Mg_4$ | $1S(a_1)$ | $1P(a_1)$+1P(e) | | | | $1S(a_1)$ | $1P(a_1)$+1P(e) | | | |
| | 3.54 | 6.62 | | | | -7.49 | -4.55 | | | |
| $Au_{20}$ | $1S(a_1)$ | $1P(a_1)$+1P(e) | $2S(a_1)$ | $1D(a_1)$+1D(e) | 1D(e) | $1S(a_1)$ | $1P(a_1)$+1P(e) | $2S(a_1)$ | $1D(a_1)$+1D(e) | 1D(e) |
| | 3.69 | 6.99 | 11.11 | 11.31 | 11.64 | -12.16 | -11.14 | -6.50 | -5.69 | -5.63 |
| $Au_{19}^-$ | $1S(a_1)$ | 1P(e) | $1P(a_1)$ | $2S(a_1)$ | 1D(e) | $1S(a_1)$ | 1P(e) | $1P(a_1)$ | $2S(a_1)$ | 1D(e) |
| | 3.60 | 6.79 | 7.15 | 10.84 | 11.00 | -9.20 | -8.19 | -8.11 | -3.23 | -2.85 |
| | 1D(e) | $1D(a_1)$ | | | | 1D(e) | $1D(a_1)$ | | | |
| | 11.37 | 12.32 | | | | -2.75 | -2.13 | | | |
| $[Al_4]^{2-}$ | $1S(a_1)$ | 1P(e) | $1P(a_1)$ | $2S(a_1)$ | 1D(e) | $1S(a_1)$ | 1P(e) | $1P(a_1)$ | $2S(a_1)$ | 1D(e) |
| | 4.00 | 6.54 | 8.08 | 10.05 | 10.32 | -1.71 | 0.65 | 2.34 | 3.98 | 4.28 |




**Supplementary Fig. 35 | Geometric structures of superatomic cores of ligand-protected gold clusters** for both GCSS and DFT calculations.

**Supplementary Table 9 | GCSS-computed results for superatomic cores of ligand-protected gold clusters** using DFT electron-density surfaces as confinement boundaries, in comparison to DFT calculations at the revTPSS/SDD level of theory.

| Superatomic core | Composition | E_GCSS (E*) | | | | | E_DFT (eV) | | | | |
|---|---|---|---|---|---|---|---|---|---|---|---|
| $[Au_{13}]^{5+}$ | $[Au_{13}(dppm)_6]^{5+}$ (ref.[80]) | 1S | $1P_{x,y}$ | $1P_z$ | | | 1S | $1P_{x,y}$ | $1P_z$ | | |
| | | 3.21 | 6.50 | 6.58 | | | -27.59 | -24.35 | -24.36 | | |
| $[Au_{20}]^{6+}$ | $[Au_{20}(PPhy_2)_{10}Cl_4]Cl_2$ (ref.[88]) | 1S | $1P_z$ | $1P_{x,y}$ | $1D_{z^2}$ | $1D_{xz,yz}$ | 1S | $1P_z$ | $1P_{x,y}$ | $1D_{z^2}$ | $1D_{xz,yz}$ |
| | | 3.31 | 5.69 | 7.21; 7.35 | 9.19 | 10.08; 10.10 | -31.58 | -30.91 | -29.33; -29.44 | -24.79 | -24.59; -24.61 |
| $[Au_{23}]^{9+}$ | $Au_{38}(SR)_{24}$ (ref. [89]) | 1S | $1P_z$ | $1P_{x,y}$ | $1D_{z^2}$ | $1D_{xz,yz}$ | 1S | $1P_z$ | $1P_{x,y}$ | $1D_{z^2}$ | $1D_{xz,yz}$ |
| | | 3.48 | 5.47 | 7.82 | 8.76 | 10.03 | -35.83 | -35.55 | -33.35 | -33.08 | -32.87 |
| $[Au_{25}]^{9+}$ | $[Au_{25}(^iPr_2\text{-bimy})_{10}Br_7]^{2+}$ (ref. [90]) | 1S | $1P_z$ | $1D_{z^2}$ | $1P_{x,y}$ | $1D_{xz,yz}$ | 1S | $1P_z$ | $1D_{z^2}$ | $1P_{x,y}$ | $1D_{xz,yz}$ |
| | | 3.70 | 5.28 | 8.14 | 8.52 | 10.13 | -39.03 | -38.50 | -37.54 | -36.47 | -31.87 |
| | | $1F_{z^3}$ | | | | | $1F_{z^3}$ | | | | |
| | | 11.65 | | | | | -31.20 | | | | |

**Supplementary Table 10 | HOMO−LUMO gaps for representative clusters** with GCSS calculations (using DFT electron-density surfaces as confinement boundaries) and DFT (revTPSS/SDD, PBE0/SDD). The energy unit is in eV.

| Cluster | $E_{H\text{-}L}$_GCSS | $E_{H\text{-}L}$_GCSS_sph. (18e; 20e) | $E_{H\text{-}L}$_revTPSS | $E_{H\text{-}L}$_PBE0 |
|---|---|---|---|---|
| $Au_{10}^{2-}$ (12e sub-shell closure in regular triangular prism potential domain) | 1.99 | 1.24; 1.85 | 1.58 | 2.60 |
| $Au_{13}^{-}$ (14e sub-shell closure in $C_{3v}$-symmetric potential domain) | 1.65 | 1.13; 1.69 | 1.52 | 2.63 |
| $Au_{20}$ (20e shell closure in regular tetrahedron potential domain) | 2.20 | 0.92; 1.37 | 1.80 | 2.97 |
| $Au_{17}^{-}$ (18e shell closure in the core-shell quasi-spherical domain) | 0.68 | 0.98; 1.46 | 1.25 | 2.22 |

Note: The GCSS model does not account for relativistic effects or electron-electron interactions.

# References


57. Zhang, H., Wu, H., Jia, Y., Geng, L., Luo, Z., Fu, H.*, et al.* An integrated instrument of DUV-IR photoionization mass spectrometry and spectroscopy for neutral clusters. *Rev. Sci. Instrum.* **90**, 073101 (2019).
58. Zhao, J., Shi, R., Sai, L., Huang, X., Su, Y. Comprehensive genetic algorithm forab initioglobal optimisation of clusters. *Mol. Simul.* **42**, 809−819 (2016).
59. Frisch, M. J., Trucks, G. W., Schlegel, H. B., Scuseria, G. E., Robb, M. A., Cheeseman, J. R.*, et al. Gaussian 16 rev. B.01*. Gaussian, Inc.: Wallingford, CT, 2016.
60. Du, Q., Wu, X., Wang, P., Wu, D., Sai, L., King, R. B.*, et al.* Structure evolution of transition metal-doped gold clusters M@$Au_{12}$ (M = 3d–5d): Across the periodic table. *J. Phys. Chem. C* **124**, 7449−7457 (2020).
61. Dolg, M., Wedig, U., Stoll, H., Preuss, H. Energy-adjusted ab initio pseudopotentials for the first row transition elements. *J. Chem. Phys.* **86**, 866−872 (1987).
62. Reed, A. E., Weinstock, R. B., Weinhold, F. Natural population analysis. *J. Chem. Phys.* **83**, 735−746 (1985).
63. Lu, T., Chen, F. Multiwfn: A multifunctional wavefunction analyzer. *J. Comput. Chem.* **33**, 580−592 (2012).
64. Bader, R. F. W., Carroll, M. T., Cheeseman, J. R., Chang, C. Properties of atoms in molecules: Atomic volumes. *J. Am. Chem. Soc.* **109**, 7968−7979 (1987).
65. Liu, Z., Lu, T., Chen, Q. Intermolecular interaction characteristics of the all-carboatomic ring, cyclo[18]carbon: Focusing on molecular adsorption and stacking. *Carbon* **171**, 514−523 (2021).
66. Humphrey, W., Dalke, A., Schulten, K. VMD: Visual molecular dynamics. *J. Mol. Graph.* **14**, 33−38 (1996).
67. Brack, M. The physics of simple metal clusters: Self-consistent jellium model and semiclassical approaches. *Rev. Mod. Phys.* **65**, 677−732 (1993).
68. Li, W.-K., Blinder, S. M. Solution of the schrödinger equation for a particle in an equilateral triangle. *J. Math. Phys.* **26**, 2784−2786 (1985).
69. Kereselidze, T., Tchelidze, T., Kezerashvili, R. Y. Energy levels of a particle confined in an ellipsoidal potential well. *Physica E* **68**, 65−71 (2015).
70. Häkkinen, H., Yoon, B., Landman, U., Li, X., Zhai, H.-J., Wang, L.-S. On the electronic and atomic structures of small $Au_n^-$ ($n$ = 4−14) clusters: a photoelectron spectroscopy and density-functional study. *J. Phys. Chem. A* **107**, 6168−6175 (2003).
71. Yin, B., Luo, Z. Coinage metal clusters: From superatom chemistry to genetic materials. *Coord. Chem. Rev.* **429**, 213643 (2021).
72. Leopold, D. G., Ho, J., Lineberger, W. C. Photoelectron spectroscopy of mass-selected sodium, coinage metal and divalent metal cluster anions. *J. Chem. Phys.* **86**, 1715–1726 (2007).
73. Bulusu, S., Li, X., Wang, L.-S., Zeng, X. C. Evidence of hollow golden cages. *Proc. Natl. Acad. Sci. U. S. A.* **103**, 8326−8330 (2006).
74. Huang, W., Wang, L.-S. Probing the 2d to 3d structural transition in gold cluster anions using argon tagging. *Phys. Rev. Lett.* **102**, 153401 (2009).
75. Li, J., Li, X., Zhai, H. J., Wang, L. S. $Au_{20}$: A tetrahedral cluster. *Science* **299**, 864−867 (2003).
76. Zhao, J. J., Du, Q. Y., Zhou, S., Kumar, V. Endohedrally doped cage clusters. *Chem. Rev.* **120**, 9021−9163 (2020).
77. Shichibu, Y., Konishi, K. Hcl-induced nuclearity convergence in diphosphine-protected ultrasmall gold clusters: A novel synthetic route to "magic-number" $Au_{13}$ clusters. *Small* **6**, 1216−1220 (2010).
78. Sugiuchi, M., Shichibu, Y., Nakanishi, T., Hasegawa, Y., Konishi, K. Cluster–π electronic interaction in a superatomic $Au_{13}$ cluster bearing sigma-bonded acetylide ligands. *Chem. Commun. (Cambridge, U. K.)* **51**, 13519−13522 (2015).
79. Sheong, F. K., Zhang, J.-X., Lin, Z. An $[Au_{13}]^{5+}$ approach to the study of gold nanoclusters. *Inorg. Chem.* **55**, 11348−11353 (2016).
80. Zhang, S. S., Feng, L., Senanayake, R. D., Aikens, C. M., Wang, X. P., Zhao, Q. Q.*, et al.* Diphosphine-protected ultrasmall gold nanoclusters: Opened icosahedral $Au_{13}$ and heart-shaped $Au_8$ clusters. *Chem. Sci.* **9**, 1251–1258 (2018).
81. Narouz, M. R., Takano, S., Lummis, P. A., Levchenko, T. I., Nazemi, A., Kaappa, S.*, et al.* Robust, highly luminescent $Au_{13}$ superatoms protected by n-heterocyclic carbenes. *J. Am. Chem. Soc.* **141**, 14997–15002 (2019).
82. Suyama, M., Takano, S., Tsukuda, T. Synergistic effects of Pt and Cd codoping to icosahedral $Au_{13}$ superatoms. *J. Phys. Chem. C* **124**, 23923−23929 (2020).
83. Shen, H., Xiang, S., Xu, Z., Liu, C., Li, X., Sun, C.*, et al.* Superatomic $Au_{13}$ clusters ligated by different n-heterocyclic carbenes and their ligand-dependent catalysis, photoluminescence, and proton sensitivity. *Nano Res.* **13**, 1908−1911 (2020).

84. Bevilacqua, M., Roverso, M., Bogialli, S., Graiff, C., Biffis, A. From $Au_{11}$ to $Au_{13}$: Tailored synthesis of superatomic Di-NHC/$PPh_3$-stabilized molecular gold nanoclusters. *Inorg. Chem.* **62**, 1383−1393 (2023).
85. Buschmann, D. A., Hirai, H., Tsukuda, T. Tuning photoluminescence properties of au clusters by surface modification and doping: Lessons from case studies of icosahedral $Au_{13}$. *Inorg. Chem. Front.* **11**, 6694−6710 (2024).
86. Zhai, X. J., Luo, M. Y., Luo, X. M., Cheng, D., Guo, M., Sun, K. X.*, et al.* Visualization of total synthesis from $Au_{11}$ to $Au_{13}$ nanoclusters. *J. Am. Chem. Soc.* **147**, 32560−32570 (2025).
87. Genest, A., Krüger, S., Gordienko Alexei, B., Rösch, N. Gold-thiolate clusters: A relativistic density functional study of the model species $Au_{13}(SR)_n$, R= h, $CH_3$, $n$ = 4,6,8. *J. Chem. Phys.* **59B**, 1585–1599 (2004).
88. Yuan, Y., Cheng, L., Yang, J. Electronic stability of phosphine-protected $Au_{20}$ nanocluster: Superatomic bonding. *J. Phys. Chem. C* **117**, 13276–13282 (2013).
89. Cheng, L., Ren, C., Zhang, X., Yang, J. New insight into the electronic shell of $au_{38}(SR)_{24}$: A superatomic molecule. *Nanoscale* **5**, 1475 (2013).
90. Shen, H., Deng, G., Kaappa, S., Tan, T., Han, Y. Z., Malola, S.*, et al.* Highly robust but surface-active: An n-heterocyclic carbene-stabilized $au_{25}$ nanocluster. *Angew. Chem. Int. Ed.* **58**, 17731−17735 (2019).